Sphingolipid imbalance aggravates tau pathology by endomembrane rigidification and rupture

Jessica Tittelmeier[1], Carl Alexander Sandhof[2,3], Nicole Martin[1], Deike El-Kabarity[1], Soki-Bradel Ngonza-Nito[4], Ronald Melki[4] and Carmen Nussbaum-Krammer[1,2,*]

[1]Chair of Neuroanatomy, Institute of Anatomy, Faculty of Medicine, Ludwig-Maximilians University of Munich (LMU), Pettenkoferstrasse 11, 80336 Munich, Germany

[2]Center for Molecular Biology of Heidelberg University (ZMBH) and German Cancer Research Center (DKFZ), DKFZ-ZMBH Alliance, Im Neuenheimer Feld 282, 69120 Heidelberg, Germany

[3]Chemical Neurobiology Laboratory, Center for Genomic Medicine, Departments of Neurology and Psychiatry, Massachusetts General Hospital and Harvard Medical School, Boston, MA 02114, USA

[4]Institute Francois Jacob (MIRCen), CEA, and Laboratory of Neurodegenerative Diseases, CNRS, Fontenay-Aux-Roses, France

*Correspondence should be addressed to carmen.nussbaum@med.uni-muenchen.de

Summary

Endolysosomal dysfunction is a hallmark of Alzheimer's disease (AD) and related tauopathies, yet underlying mechanisms remain poorly understood. This study investigates the role of sphingolipid metabolism in maintaining endolysosomal membrane integrity and its impact on tau aggregation and toxicity in *Caenorhabditis elegans* and human cell culture models. Fluorescence recovery after photobleaching and C-Laurdan dye imaging revealed that silencing sphingolipid metabolism genes reduced endolysosomal vesicle membrane fluidity, increasing their rupture. The accumulation of aggregated tau in endolysosomal vesicles further aggravated endomembrane rigidification and damage and promoted seeded tau aggregation, potentially by facilitating the escape of tau seeds from the endolysosomal system. Supplementation with unsaturated fatty acids improved membrane fluidity, suppressing endolysosomal rupture and seeded tau aggregation in cell models, and alleviating tau-associated neurotoxicity in *C. elegans*. This study provides mechanistic insights into how impaired sphingolipid homeostasis drives endolysosomal membrane damage and contributes to the progression of tau pathology, suggesting that restoring membrane fluidity may offer a therapeutic strategy for AD.

Keywords: Alzheimer's disease / tau propagation / sphingolipid metabolism / endolysosomal system / lipid homeostasis

Introduction

The gradual accumulation of microtubule-associated protein tau (MAPT/tau) aggregates is a hallmark of Alzheimer's disease (AD) and related tauopathies. Misfolded tau species exhibit prion-like behavior by self-replicating and spreading from cell to cell[1,2]. This contributes to the progression of pathology and neurotoxicity, eventually culminating in widespread neuronal dysfunction and degeneration[3]. At the molecular level, tau aggregates replicate by templating the conversion of native tau into an amyloid conformation, promoting its accumulation into fibrillar aggregates. For this to occur at the cellular level, seeding-competent tau species (or tau "seeds") must be released from a donor cell and taken up into the cytosol of the neighboring receiving cell in order to come into direct contact with the cytosolic native tau protein[4-6].

In this process, the autophagy-lysosomal pathway (ALP), which is an important clearance route for tau[7], appears to play a central role. Studies have demonstrated impaired ALP function in the brains of tauopathy patients as well as in animal and cell models, showing that the accumulation of abnormal autolysosomal and endolysosomal vesicles correlating with neuronal toxicity[8-11]. Inhibition of autophagic clearance of tau increases its secretion and spreading[12]. In addition, the accumulation of misfolded tau within endolysosomes leads to a destabilization and rupture of these vesicles[13-18]. While intact endolysosomes normally restrict tau seeds from reaching cytosolic monomers, membrane rupture allows their escape. Recent studies highlight this escape as a critical rate-limiting step in seeded tau propagation[13-18]. Endolysosomal damage not only promotes the propagation of pathological aggregates, but also causes the release of hydrolytic enzymes into the cytosol, leading to cellular damage and death[19]. Although recent efforts to identify pathways involved in endolysosomal damage and repair have intensified, many aspects of these processes remain unknown.

To identify cellular factors that are critical for the integrity of endolysosomal vesicles, we recently performed an unbiased genome-wide RNAi screen in *C. elegans*[20]. One of the pathways identified was sphingolipid (SL) metabolism. SLs constitute a large and diverse class of lipids that are involved in various physiological processes[21,22]. They consist of two main building blocks, a long-chain base with a serine backbone and an attached long acyl chain. This characteristic chemical structure mediates unique biophysical properties. SL biosynthesis and degradation rely on a specialized enzymatic machinery distinct from that of other lipids[23] (Figure 1A). Functionally, SLs, along with glycerolipids and sterols, serve as structural components of cell membranes,

contributing to the stability and fluidity of membranes and to the organization of microdomains such as lipid rafts. Beyond their structural role, SLs serve as bioactive molecules participating in cellular signaling pathways that control cell growth, differentiation, apoptosis, and intercellular communication[24]. Abnormalities in SL metabolism have been observed during aging and in neurodegenerative conditions, including AD, underscoring their potential significance in the pathogenesis of these disorders[25,26]. Interestingly, recent evidence suggests that sphingolipid accumulation disturbs the endolysosomal pathway and induces or potentiates endolysosomal membrane rupture[27,28]; however, the mechanisms underlying membrane destabilization remain unclear.

Here we investigated the role of SL metabolism in the maintenance of endolysosomal vesicle integrity. Our results revealed that silencing of SL metabolism genes led to a marked reduction in membrane fluidity, particularly in endolysosomal vesicles, thereby increasing their fragility and rupture. The accumulation of aggregated tau had an additive effect and led to a further reduction in endomembrane fluidity, which aggravated the damage to the endolysosomal compartment. Increased membrane rigidity also facilitated seeded tau aggregation. Improvement of membrane fluidity through supplementation of polyunsaturated fatty acids (PUFAs) counteracted tau propagation in cells and tau-associated neurotoxicity in *C. elegans*.

This study highlights the interplay between lipid metabolism and proteostasis and provides insights into how disturbances in sphingolipid homeostasis contribute to endolysosomal dysfunction and tau pathology. In addition, it provides a possible mechanistic explanation for the beneficial effect of PUFA supplementation that has been observed in AD patients and suggests that restoring membrane fluidity may help mitigate tau toxicity and disease progression.

100 **Results**

101 **Knockdown of sphingolipid metabolism genes induces lysosomal rupture**

102 Several of the strongest hits identified in the unbiased genome-wide RNAi screen we performed
103 to identify modulators of endolysosomal vesicles integrity were genes involved in SL metabolism
104 (Figure 1A). Knockdown (KD) of these genes (the serine incorporator *R11H6.2*, the 3-
105 ketodihydrosphingosine reductase *Y37E11AM.3,* the hydroxyacyl-CoA dehydratase *hpo-8*, the
106 cytochrome b5 reductases *hpo-19* and *T05H4.4,* the saposin *spp-10*, the sphingosine kinase *sphk-*
107 *1*, and the sphingosine-1-phosphate lyase *spl-1*) via RNA interference (RNAi) induced
108 endolysosomal membrane damage as detected by a galectin puncta assay[29] (Figure 1B-D). Under
109 steady-state conditions, human galectin-3 fused to superfolder-GFP (sfGFP::LGALS3) exhibits an
110 even distribution within the cytosol of hypodermal cells. Upon endolysosomal vesicle damage and
111 exposure of their lumen to the cytosol, sfGFP::LGALS3 binds exposed β-galactoside and re-
112 localizes, yielding visible puncta[29].

113 The screen identified distinct steps in sphingolipid metabolism catalyzed by non-redundant genes
114 or targeted by a single RNAi clone, as in the case of *hpo-19*/*T05H4.4* which are both depleted by
115 *hpo-19* RNAi. However, other steps in this pathway, which are mediated by two or more proteins
116 may have been missed in the screen. Indeed, simultaneous KD of selective redundant genes using
117 co-RNAi revealed additional genes functioning in *de novo* sphingolipid biosynthesis that also
118 induced endolysosomal rupture, including the serine palmitoyltransferases *sptl-1* and *-3* and the
119 ceramide synthases *hyl-1* and *-2* (Figure S1A). In addition, the co-KD of all four
120 glucocerebrosidases *gba-1-4* or only *gba-2-4*, also triggered endolysosomal rupture (Figure S1B).
121 Hence, these findings suggest that the KD of genes involved in both biosynthesis and degradation
122 of SLs contributes to endolysosomal rupture, highlighting the tightly regulated nature of
123 sphingolipid metabolism. Any disruption in this balance poses challenges to endolysosomal
124 integrity.

125

126 **KD of sphingolipid metabolism genes particularly affects membrane fluidity of**
127 **endolysosomal vesicles**

128 SLs are important components of eukaryotic cell membranes and genetic modulation of SL
129 metabolism likely affects the lipid composition and biophysical properties of membranes. Similar
130 to their mammalian isoforms, the N-acyl chains of *C. elegans* SLs contain predominantly long and

131 saturated fatty acid chains[30,31], which tend to pack tightly within the lipid bilayer. As such, a higher
132 proportion of SLs generally reduces membrane fluidity, leading to increased order, rigidity, or
133 viscosity[32]. Consequently, KD of the hits involved in SL degradation should lead to SL
134 accumulation and reduced membrane fluidity, while KD of the hits involved in SL biosynthesis
135 should have the opposite effect.
136 To evaluate the membrane fluidity of endolysosomal membranes, fluorescence recovery after
137 photobleaching (FRAP) was employed on *C. elegans* that express the Lysine/Arginine Transporter
138 1 (LAAT-1) tagged with mCherry, which localizes to the lysosomal membrane[33]. FRAP enables
139 the assessment of the lateral mobility of LAAT-1 within the lysosomal membrane, thereby
140 indirectly measuring its fluidity. We focused our analysis on the hypodermis, where we expressed
141 the sfGFP::LGALS3 reporter and observed endolysosomal rupture following KD of the SL
142 metabolism genes (Figure 1C, D). Interestingly, KD of all of our hits significantly increased the
143 time required to recover half of the maximum fluorescence intensity (t_{half}), indicating less fluid
144 lysosomal membrane in the hypodermis (Figure 2A-C, E, F). With some gene KDs, we also
145 observed a decrease in the maximal recovered signal after bleaching (Figure 2D, G). The decrease
146 in lysosomal membrane fluidity was not specific to the hypodermis as the KD of *spl-1* also
147 increased the t_{half} of LAAT-1::mCherry in intestinal lysosomes (Figure S2A-D). To discern
148 whether the detrimental effect of KD on membrane fluidity is confined to lysosomal membranes
149 or extends to other cellular membranes, we utilized a *C. elegans* strain expressing a plasma
150 membrane-anchored GFP[34]. Intriguingly, this reporter showed no change in the t_{half} with any KD
151 and only *spl-1* KD led to decrease in the maximal recovered signal (Figure 2H-K). Hence, the
152 endolysosomal membrane seems to be particularly sensitive to a disruption of SL metabolism in
153 contrast to the plasma membrane. Dysregulation of both, synthesis and degradation of SLs reduces
154 the fluidity of the endolysosomal membrane and makes it more susceptible to rupture.
155
156 **KD of sphingolipid metabolism genes affects membrane fluidity in human cells**
157 Next, we asked whether dysregulation of SL metabolism exerts similar effects in human cells. To
158 this end, we employed HEK293T cells and C-Laurdan dye to evaluate membrane fluidity (Figure
159 3A). This approach leverages the unique properties of C-Laurdan, which emits fluorescent light of
160 varying wavelengths in response to changes within the phospholipid bilayer, particularly reflective
161 of membrane fluidity[35,36]. The shift in emission profile between liquid-disordered and liquid-

162 ordered phases allows a quantitative assessment of the membrane order by calculating the
163 ratiometric relationship of the fluorescence intensity recorded in two spectral channels, known as
164 a generalized polarization (GP) value[35] (Figure 3A). Decreasing GP values are indicative of
165 increasingly fluid membrane while increasing GP values denote increased rigidity. Of note, we
166 exposed the cells to C-Laurdan for an extended time of 2 hours (instead of 30 min as recommended
167 in the original protocol), to promote internalization of the dye and thus increase the staining of
168 endolysosomal membranes relative to the plasma membrane[35]. Upon KD of *SPHK2*, one of the
169 human homologs of the *C. elegans sphk-1* gene, the C-Laurdan fluorescence GP ratio augmented
170 significantly, indicating increased membrane rigidity (Figure 3B, D and Figure S3A). Of note,
171 Lipofectamine 2000 was used to deliver siRNA into the cells and lipid-based transfection reagents
172 have been shown to impact endolysosomal membranes[37]. Indeed, Lipofectamine alone slightly
173 increased membrane fluidity (Figure 3C). Taken together, FRAP and C-Laurdan analyses revealed
174 that disrupted SL homeostasis led to more ordered and rigid endolysosomal membranes, in both
175 *C. elegans* and human cells.
176
177 **Fibrillar tau increases membrane rigidity and exacerbates endolysosomal damage**
178 To investigate whether disruption of SL homeostasis also affects endolysosomal integrity in
179 human cells, we generated a HEK293T cell line stably expressing the same sfGFP-LGALS3
180 reporter used for the galectin puncta assay in *C. elegans*. To further mimic the *C. elegans* model,
181 in which aggregation-prone tau fragments are chronically transferred from the touch receptor
182 neurons into the hypodermis where the sfGFP-LGALS3 reporter is expressed[20], recombinant
183 1N4R tau fibrils were added to sfGFP-LGALS3 expressing HEK293T cells on top of the KD of
184 *SPHK2*. Interestingly, both the addition of tau fibrils alone and the KD of *SPHK2* alone already
185 caused rupture of endolysosomes in sfGFP-LGALS3 cells (Figure 3D, E and Figure S3B). The
186 combination of both had an additive effect (Figure 3D, E and Figure S3B).
187 We therefore asked whether the KD of SLs alone would also already rupture hypodermal
188 endolysosomes in *C. elegans* and whether accumulation of transmitted tau would exacerbate this
189 process. To answer this question, we determined the amount of hypodermal sfGFP-LGALS3 foci
190 in F3$^{\Delta K281}$::mCherry *C. elegans* compared to control animals expressing only the mCherry tag. KD
191 of *Y37E11AM.3* alone did not increase lysosomal rupture compared to the EV control RNAi, only
192 the presence of tau spreading resulted in more lysosomal rupture relative to the control (Figure

193 3F). KD of the remaining hits resulted in near 100% animals with hypodermal sfGFP-LGALS3
194 foci in both the F3$^{\Delta K281}$::mCherry and mCherry control strains. To test whether the additional
195 negative impact of the F3 tau fragment might be masked by the strength of the RNAi clones,
196 different dilutions of the RNAi bacteria were tested. Under conditions where the RNAi KD did
197 not saturate the readout of the assay, KD of *spl-1, hpo-8,* and *hpo-19* alone already affected
198 lysosomal integrity (Figure 3G). Moreover, F3$^{\Delta K281}$::mCherry transgenic animals showed a
199 significantly higher level of endolysosomal rupture upon KD of *spl-1, hpo-8,* and *hpo-19* compared
200 to the mCherry control (Figure 3G). Diluting the *R11H6.2* RNAi clone showed no significant
201 differences, and KD of *sphk-1* still resulted in 100% endolysosomal rupture-positive animals in
202 both genetic backgrounds even after dilution of the RNAi bacteria to below 5% and could therefore
203 not be assessed. In conclusion, chronic transmission of the F3$^{\Delta K281}$::mCherry fragment from the
204 touch receptor neurons to the hypodermis impaired the endolysosomal system exacerbating the
205 rupture due to perturbation of SL homeostasis.
206 Since disruption of SLs metabolism led to an increase in membrane rigidity resulting in
207 endolysosomal rupture, and fibrillar tau also ruptured endolysosomal membranes (Figure 3D, E)[14],
208 we asked whether tau itself could also affect membrane fluidity. To test this, membrane fluidity
209 was assessed for somas of the posterior (PLM) touch receptor neurons of *C. elegans* using C-
210 Laurdan dye. Indeed, expression of the tau fragment led to a decrease in membrane fluidity
211 compared to expression of the mCherry tag alone (Figure 3H, I). Also, HEK293T cells incubated
212 with tau fibrils for 5 hours exhibited an increased GP index (Figure 3J, K). Importantly, this was
213 specific to fibrillar tau, as monomeric tau had no effect on membrane fluidity (Figure 3L and
214 Figure S3C). Thus, aggregated forms of tau can cause rigidification of the endolysosomal
215 membrane, resulting in increased fragility and rupture.
216
217 **Membrane rigidification exacerbates seeded tau aggregation**
218 The packing of fatty acids within the membrane influences membrane fluidity. Saturated fatty
219 acids (SFAs) have straight hydrocarbon chains forming a tightly packed, highly ordered and rigid
220 membrane. To investigate the role endomembrane lipid homeostasis plays in tau propagation, we
221 introduced an SFA to rigidify membranes. Incubating HEK293T cells with the SFA palmitic acid
222 (PA) conjugated to BSA increased membrane rigidity (Figure 4A, B). In addition, cells incubated

223 with PA and tau fibrils had an even more rigid membrane than cells incubated with tau fibrils alone
224 (Figure 4C, D).
225 An important step in tau propagation is tau seeds escape from the endolysosomal compartment,
226 which can then propagate themself by recruiting native monomeric tau. Therefore, we asked if the
227 PA-induced loss of membrane fluidity impairs endolysosomal integrity. Worms grown on plates
228 supplemented with PA displayed an increase in endolysosomal rupture (Figure 4E). In cells, the
229 addition of PA alone did not lead to endolysosomal rupture; however due to compounding impact
230 of PA and tau fibrils on membrane fluidity, the addition of PA increased fibrillar tau-induced
231 endolysosomal rupture (Figure 4F, G). Hence, loss of membrane fluidity mediated by fibrillar tau
232 and/or SFAs negatively affects endolysosomal integrity, resulting in increased endolysosomal
233 rupture.
234 Impairment of endolysosomal integrity may enhance tau propagation as tau could escape from the
235 endolysosomal compartments, reach the cytosol and recruit native monomeric tau, promoting
236 seeded tau aggregation. Given the observed membrane rigidification after pre-loading with SFAs,
237 we investigated whether membrane lipid composition influences tau propagation using a tau
238 biosensor cell line expressing Venus-tagged full-length P301S mutant 0N4R tau (tau-Venus)[38,39].
239 PA-induced membrane rigidification led to an increase in tau-Venus foci upon seeding with tau
240 fibrils (Figure 4H, I). Moreover, KD of *SPHK2* also increased the formation of tau-Venus foci due
241 to SPHK2 KD-mediated membrane rigidification (Figure S4C, D). This highlights a positive
242 correlation between membrane rigidity and seeded tau aggregation. Changes in membrane fluidity,
243 which compromise endolysosomal integrity may promote the entry of seeds into the cytosol. This
244 would consequently foster the seeded propagation of tau aggregation.
245
246 **Increasing membrane fluidity by PUFAs rescues neurotoxic phenotypes**
247 Given that membrane stiffening exacerbates tau propagation, we wondered whether we could
248 prevent this by improving membrane viscosity. While SFA allow for tightly packed lipids,
249 unsaturated fatty acids have one or more double bonds in their hydrocarbon chain that introduce
250 kinks in their structure, resulting in loosely packed lipids and increased membrane fluidity.
251 Therefore, we investigated whether we could rescue tau pathology using polyunsaturated fatty
252 acids (PUFAs). Incubating HEK293T cells with the ω-3 PUFA α-linolenic acid (ALA) increased
253 membrane fluidity (Figure 5A and Figure S5A). Moreover, pre-loading with ALA prevented tau-

254 induced membrane rigidification and decreased the GP-index of membranes even after the addition
255 of tau fibrils (Figure 5B, C). Importantly, pre-loading cells with ALA also counteracted fibrillar
256 tau-mediated endolysosomal rupture (Figure 5D, E and Figure S5B).
257 Since ALA prevented endolysosomal rupture, we expected it to also prevent seeded tau
258 aggregation. Indeed, tau-Venus cells pre-loaded with ALA exhibited significantly fewer foci when
259 exposed to tau fibrils (Figure 5F and Figure S5C). These data show that ALA supplementation
260 counteracts tau-mediated decrease in membrane fluidity, thereby preventing endolysosomal
261 rupture and decreasing seeded tau aggregation.
262 Finally, we asked whether ALA would also reduce the toxicity associated with aggregated tau.
263 Expression of $F3^{\Delta K281}$::mCherry in touch receptor neurons resulted in an age-dependent decline in
264 the response to gentle touch from day 4, corresponding to the first day of adulthood to day 8,
265 corresponding to day 5 of adulthood (Figure 5H, and Figure S5D)[20]. Addition of ALA to the
266 growth medium mitigated this loss of function (Figure 5H and Figure S5D) and also reduced
267 neurotoxicity (Figure 5I, J). Thus, supplementation with ALA not only reduced endolysosomal
268 damage but also attenuated neurotoxic phenotypes associated with aggregated tau.
269
270

271 **Discussion**

272 In a previous genome-wide screen in *C. elegans*, we identified genes involved in SL metabolism
273 as crucial for maintaining endolysosomal integrity[20]. In this study we explored the mechanisms by
274 which disruption of SL homeostasis leads to endolysosomal rupture and how it affects tau
275 pathology. We found that imbalanced SL metabolism leads to decreased membrane fluidity, and
276 subsequent endolysosomal rupture. This promoted seeded tau aggregation in a biosensor cell line
277 exposed to fibrillar tau, implying that dysregulation of SL metabolism might boost disease
278 progression by enhancing propagation of tau aggregation.

279 The central nervous system (CNS) is particularly rich in lipids. Approximately 50% of the brain's
280 dry weight consists of lipids with high concentrations of cholesterol, phospholipids and
281 sphingolipids [40,41]. Alterations in lipid and SL metabolism have been observed not only during the
282 aging process, but also in various late-onset neurodegenerative diseases including AD[26,42]. While
283 aging is the major risk factor for AD, one of the most significant genetic risk factors for AD is the
284 apolipoprotein E (ApoE) polymorphism, specifically the ApoE4 allele[43]. ApoE is the primary
285 lipoprotein in the brain, crucial for lipid transport and metabolism. Besides cholesterol, the ApoE4
286 variant has been shown to influence SL metabolism, thereby affecting the pathogenesis of AD
287 from its early stages[26,42,44]. While disturbances in SL homeostasis are increasingly recognized as a
288 contributing factor to the onset and progression of the disease[26,42], the underlying mechanisms are
289 poorly understood.

290 Our results show that reducing the expression of genes involved in both, biosynthesis and
291 degradation of SLs significantly reduced the fluidity of endolysosomal membranes, making them
292 more fragile and prone to rupture. KD of the saposin *spp-10*, the sphingosine kinase *sphk-1*, and
293 the sphingosine-1-phosphate lyase *spl-1* blocks the degradation of complex SLs and should lead
294 to an increase in their relative abundance, and therefore to a decrease in membrane fluidity. KD of
295 the very-long-chain (3R)-3-hydroxyacyl-CoA dehydratase *hpo-8*, which is involved in fatty acid
296 elongation, has been demonstrated to promote the incorporation of long-chain UFAs into
297 phospholipids, thereby restoring plasma membrane fluidity[45]. The absence of *hpo-8* leads to
298 membrane rigidification[45]. Conversely, KD of the serine incorporator *R11H6.*2 and the 3-
299 ketodihydrosphingosine reductase *Y37E11AM.3*, which function in the SL de novo synthesis
300 pathway, should theoretically decrease total SL content and consequently increase membrane
301 fluidity. The cytochrome b5 reductases *hpo-19* and *T05H4.4*, required for lipid desaturation, are

302 involved in the conversion of dihydroceramide to ceramide and the biosynthesis of PUFAs[46]; KD
303 of these genes is expected to reduce the levels of SLs and PUFAs, which could theoretically either
304 increase or decrease membrane fluidity, depending on which metabolic pathway is predominantly
305 affected.
306 Our observation that KD of all these genes results in decreased membrane fluidity is seemingly
307 counterintuitive. However, SLs form a complex metabolic network and can interconvert, allowing
308 a dynamic adaptation of SL levels. In addition, the cell likely compensates for the loss of certain
309 SLs by increasing the biosynthesis of other lipid molecules. This dynamic interplay makes it
310 difficult to predict how individual genes affect the endolysosomal membrane lipid composition.
311 Genes that are involved in apparently opposing steps of SL metabolism could therefore still lead
312 to an accumulation of similar SL species.
313 Future lipidomic analyses are necessary to determine the SL and lipid content of endolysosomal
314 membranes in our model systems. Such studies will provide a clearer understanding of how genetic
315 manipulation of SL metabolism affects endomembrane lipid composition and could pinpoint the
316 exact species likely responsible for the observed membrane rigidification.
317 AD brains exhibit elevated levels of sphingosine, ceramide 1-phosphate, and ceramide compared
318 to control subjects[42]. Multivariate analysis and machine learning also identified these SL species
319 as key contributors to AD[42]. These and other analyses were performed in different brain regions
320 but without cell type or subcellular resolution. We found that disruption of *C. elegans* SL
321 homeostasis primarily affected endolysosomal membranes and had little effect on plasma
322 membrane fluidity. The lysosomal membrane is particularly rich in sphingolipids[47], which seems
323 to make it more susceptible to disruption of SL homeostasis. Studies in yeast have shown that
324 increased membrane lipid saturation affects the vacuole —the functional counterpart of
325 mammalian lysosomes—as well as the nuclear envelope, whereas the plasma membrane and
326 mitochondria remained relatively unaffected[48]. These findings indicate that cellular membranes
327 vary in their resilience to lipid saturation stress, potentially due to differences in lipid composition
328 and protective mechanisms[48,49]. To better understand the implications of SL alterations in AD, it
329 would be important to examine whether the observed changes primarily originate from
330 endolysosomal membranes or also from other organelles, such as the endoplasmic reticulum and
331 the nucleus, or from the plasma membrane.

332 Intriguingly, expression of the aggregation-prone F3 tau fragment also enhanced membrane
333 rigidity with SL homeostasis disruption having an additive effect, exacerbating endomembrane
334 damage. Thus, alterations in SL metabolism could be not only a cause but also a consequence of
335 AD related pathology[26,42]. The accumulation of misfolded tau in lysosomes could impair the
336 lysosomal clearance capacity. This dysfunction may reduce the activity of acid hydrolases, leading
337 to an accumulation of biomolecules, including membrane lipids. Impairment of membrane lipid
338 metabolism could in turn further compromise lysosomal integrity and function. Both processes -
339 accumulation of SLs and protein aggregates - may create a vicious self-promoting cycle of
340 lysosomal dysfunction that eventually leads to neurodegeneration.
341 Supplementation of SFAs exacerbated the negative impact of the F3 tau fragment on
342 endomembrane fluidity. Given the high levels of saturated and trans fats in the Western diet[50], it
343 is plausible that dietary factors also contribute to the dysregulation of lipid homeostasis in the
344 brain. The Mediterranean UFA-rich diet has been associated with healthy aging, while reduced
345 UFA brain levels have been correlated with increased tau and Aβ pathology and decreased
346 cognitive function in AD[51,52]. Restoring membrane fluidity through the supplementation of PUFAs
347 mitigated tau propagation in cells and reduced tau-associated neurotoxicity in *C. elegans*. These
348 results suggest a potential mechanism for the beneficial effects of PUFA supplementation observed
349 in AD patients[53,54]. Future studies are needed to evaluate whether these benefits are related to an
350 increase in the fluidity of endolysosomal membranes and the consequent prevention of their
351 damage by protein aggregates and/or impaired SL homeostasis.
352 In sum, this study revealed an important role of endolysosomal membrane homeostasis in disease
353 progression providing a possible mechanism for the detrimental effect of SL imbalance and
354 beneficial effect of PUFA supplementation that have been observed in AD patients.
355
356

357 **Methods**

358 **Maintenance of *C. elegans* and age synchronization**

359 All animals were cultured using standard methods[55]. If not otherwise indicated, worms were grown
360 on nematode growth medium (NGM) plates seeded with *E. coli* strain OP50 at 20 °C. For RNAi,
361 NGM medium were supplemented with Ampicillin, Tetracycline, and IPTG, seeded with the
362 respective HT115 *E. coli* RNAi clones and grown at 20 °C. Animals were age-synchronized by
363 bleaching. Briefly, gravid adults were dissolved in 20% sodium hypochlorite solution. The
364 surviving *C. elegans* embryos were hatched overnight in M9 buffer with gentle rocking at 20 °C.
365 The next day, appropriate amounts of L1 larvae were added to the plates.

366

367 ***C. elegans* fatty acid supplementation**

368 Polyunsaturated fatty acids were dissolved in EtOH and stored in the dark at -20 °C under a N_2
369 atmosphere to prevent oxidation. NGM was cooled after autoclaving to 55 °C. To enhance fatty
370 acid distribution, NP-40 substitute (0.001% v/v) was added to the media and subsequently either
371 0.3 mM of the desired fatty acid solution or the ethanol solvent as control and stirred for 5 min
372 before plate pouring [56]. Palmitic acid (PA) was supplemented by enriching the OP50 bacterial food
373 source. Overnight cultures were grown in the presence of 2 mM of PA dissolved in EtOH or EtOH.
374 The next day, OP50 bacteria were pelleted by centrifugation (10 min at 4500x g) and washed 2x
375 with M9 buffer[57]. 10x concentrated bacteria (in M9) were then seeded on NGM plates.

376

377 **Quantification of lysosomal rupture (galectin puncta assay) in *C. elegans***

378 Quantification of animals showing hypodermal lysosomal rupture was done as previously
379 described[29,58]. Briefly, age-synchronized animals expressing the sfGFP::LGALS3 construct in the
380 hypodermis were seeded on OP50 or RNAi NGM plates. Scoring was done using a Leica M205
381 FA widefield binocular microscope. 20-50 worms were analyzed per replicate.

382

383 **Mounting of live animals for imaging**

384 Synchronized animals were mounted on 8-10% agarose in M9 buffer pads with a drop of mounting
385 mix (2% (w/v) levamisole and 50% (v/v) nanosphere size standards (Thermo Fisher)) and covered
386 with a coverslip.

387

388 **Fluorescence recovery after photobleaching (FRAP)**

389 FRAP measurements to estimate membrane fluidity were done following a published protocol[59].
390 Animals were synchronized by bleaching and grown until the second day of adulthood on the
391 indicated RNAi or empty vector (EV) control plates. Directly before the FRAP experiments,
392 animals were mounted at the Zeiss LSM 780 confocal microscope. FRAP measurements of either
393 GFP enriched in the intestinal plasma membrane, or LAAT-1::mCherry located in intestinal or
394 hypodermal lysosomal membranes were taken with 40X Water immersion objective. For the
395 lysosomal membrane, mCherry-positive membranes were photobleached over a circular area
396 (seven pixel radius) using 10 iterations of the 561 nm DPSS laser with 100% laser power
397 transmission. Images were collected at a 12-bit intensity resolution over 128 × 128 pixels (digital
398 zoom 6X) using a pixel dwell time of 3.15 µsec with 2% laser power transmission. For the plasma
399 membrane, GFP-positive membranes were photobleached over a circular area (10 pixel radius)
400 using 20 iterations of the 488 nm Argon laser with 100% laser power transmission. Images were
401 collected at a 12-bit intensity resolution over 128 × 128 pixels (digital zoom 6X) using a pixel
402 dwell time of 3.15 µsec with 10% laser power transmission. At least 6 pre-bleaching images were
403 collected before the region of interest was bleached. The recovery of fluorescence was traced for
404 25s. Fluorescence recovery and T_{half} were calculated as previously described in Svensk et al.[60].
405

406 **Touch sensory assay and neurotoxicity in touch receptor neurons**

407 Touch sensory assay was done as previously described[61]. Briefly, touch sensitivity was tested by
408 gently stroking the tip of an eyebrow hair attached to a toothpick transversely across the anterior
409 or posterior half of an animal. A touch-sensitive animal was one that stopped/moved away from
410 the stimulus. 10 worms were examined for each strain in 3 biological replicates with 5 strokes in
411 the anterior and posterior. For neurotoxicity scoring of the PLM neurons, live animals were imaged
412 using an Olympus IXplore SpinSR Confocal microscope with an UplanS Apo 60x/1.30 Silicon oil
413 objective. The neurotoxicity score was determined by adding a score of 1 for each of the following
414 phenotypes: soma outgrowth, process branching, process break, wavy process. 15 animals were
415 examined at each day of age in 3 independent biological replicates.
416
417
418

419 **Cell culture**

420 Cells were cultured in DMEM containing high glucose, GlutaMAX Supplement, pyruvate (Gibco),
421 and 10% FBS (Gibco) at 37 °C and 5% CO_2. Regular mycoplasma tests were performed (GATC
422 Biotech). HEK293T cells expressing Venus-tagged full-length P301S mutant 0N4R tau (0N4R
423 tauP301S-Venus) were kindly provided by Dr. William A. McEwan, Cambridge University[38].

424

425 **Cloning of mammalian expression constructs and generation of sfGFP-LGALS3 HEK293T**
426 **cells**

427 HEK293T cells were cultured in DMEM containing high glucose, GlutaMAX supplement,
428 pyruvate (Gibco), and 10% FBS (Gibco) at 37 °C and 5% CO_2. Cells expressing sfGFP-LGALS3
429 were generated as follows. sfGFP::LGALS3 was amplified from the *C. elegans* expression plasmid
430 pPD49.26 by PCR and cloned into the pLenti PGK Puro DEST (w529-2) vector backbone
431 (Addgene plasmid #19068) by MultiSite Gateway cloning according to the manufacturers
432 protocol. pLenti PGK Puro DEST (w529-2) was a gift from Eric Campeau & Paul Kaufman[62].
433 After each cloning step plasmids isolated from bacterial colonies grown on selective media were
434 extracted with the GenEluteTM Five-Minute Plasmid Miniprep Kit (Qiagen) and validated by
435 sequencing. HEK293T sfGFP-LGALS3 were generated using a 3rd generation lentiviral system.
436 Lentivirus was produced by transiently transfecting HEK293T cells with the pLenti PGK Puro
437 DEST, MDL-gagpol, RSV-REV and IVS-VSVG at a ratio of 5:3:1:1, respectively. Cell media was
438 changed 24 hours after transfection. Viral supernatant was collected 72 h post-transfection. After
439 centrifugation at 2000 x g for 5 min, the supernatant containing the virus was concentrated by
440 adding the PEG-it Virus Precipitation Solution (Systems Biosciences) followed by overnight
441 incubation at 4 °C. The precipitated virus was pelleted by centrifugation (1500 x g, 30 min, 4°C),
442 resuspended in DMEM containing 25 mM HEPES buffer and stored at -80 °C. The lentivirus was
443 added to HEK293T followed by treatment with Puromycin to select successfully transduced
444 HEK293T cells stably expressing sfGFP-LGALS3.

445

446 **Quantification of lysosomal rupture (galectin puncta assay) in cells**

447 Cells were imaged on an Olympus IXplore SpinSR Confocal microscope with an UplanS Apo
448 60x/1.30 Silicon oil objective. To detect the number of foci in an image, a difference of gaussian
449 blur was applied to max projections to isolate foci from cytsosolic sfGFP signal. Thresholding was

450 applied using 'moments' threshold on FIJI. Number of foci was counted using the 'analyze
451 particles' function. Cell number was counted manually to obtain number of foci/cell for each
452 image.
453
454 **C-Laurdan dye measurement of membrane fluidity in worms and cells**
455 Live worms were stained with 10 mM C-Laurdan dye (6-dodecanoyl-2-
456 dimethylaminonaphthalene) (Thermo Fisher Scientific) as previously described[63]. Cells were also
457 stained with C-Laurdan at 15 μM for 2 hours then fixed in 4% PFA in PBS. Images were acquired
458 with an DMI6000 confocal microscope and Leica software with a 63x oil-immersion objective,
459 with a zoom factor of 4. Samples were excited with a 405 nm laser and the emission recorded
460 between 400 and 460 nm (ordered phase) and between 470 and 530 nm (disordered phase).
461 Quantitative assessment of the membrane order was achieved by calculating the ratiometric
462 relationship of the fluorescence intensity recorded in two spectral channels (GP value) by using an
463 automated ImageJ macro, according to published guidelines[35].
464
465 **Knockdown of target genes by RNAi in cells**
466 SPHK2 or a scrambled control siRNA was purchased from Thermo Scientific Dharmacon
467 (ONTarget plus siRNA and Control Pool). Cells were seeded in DMEM with 10% FBS. siRNA
468 was diluted in siRNA buffer (Final concentration 20 nM) before mixing with Lipofectmine2000
469 for 20 min prior to being added to cells. To minimize lipofectamine impact on the endolysosomal
470 system, media was exchanged after 6 hours.
471
472 **SDS-Page and immunoblotting.**
473 Cells were pelleted by centrifugation followed by lysis in lysis buffer (10mM Tris, 100mM NaCl,
474 0.2% Triton X-100, 10mM EDTA) on ice for 20 min. The lysates were transferred into fresh
475 Eppendorf tubes and centrifuged (1000 g for 1 min at 4 °C) in a tabletop centrifuge to remove
476 cellular debris. The protein concentration was determined using protein assay dye reagent
477 concentrate (Bio-Rad). Proteins were separated under denaturing conditions by SDS–PAGE and
478 transferred onto a PVDF membrane (Carl Roth) by standard wet blotting protocols. Samples were
479 probed with rabbit polyclonal anti-SPHK2 (1:5000, 9C5E1, Santa Cruz) primary antibody. Anti-
480 GAPDH antibody (1:5000, clone GAPDH-71.1, Sigma-Aldrich) was used as loading control.

481 HRP-conjugated anti-mouse and anti-rabbit IgG secondary antibodies (Bio-Rad) were used for
482 subsequent ECL-based detection (Bio-Rad).
483
484 **Fatty acid treatment in cells**
485 For α-linolenic acid (ALA), a stock solution was made in EtOH and stored in the dark at -20°C
486 under a N_2 atmosphere to prevent oxidation[64]. Palmitic acid (PA) was dissolved in 0.1 M NaOH
487 according to Cousin et al.[65]. ALA and PA were then conjugated to BSA in 10% fatty acid free
488 solution by shaking for 1 hour at 37°C to a concentration of 6 mM for ALA and 5 mM for PA[66].
489 Prior to preloaded cells with BSA-PA, the solution was heated to 65 °C for 15 min. For assays
490 with C-Laurdan, cells were preloaded with FAs for 3 hours before the addition of C-Laurdan for
491 another 2 hours. If preloading was followed by seeding with tau, preloading with FAs was done
492 for 3 hours before fibrillar tau was added for an additional 5 hours. C-Laurdan was spiked in for
493 the last 2 hours. No media changes were done between steps. For experiments with HEK293T tau-
494 Venus cells and HEK293T sfGFP-LGALS3 cells, preloading with FAs was done for 3 hours before
495 seeding with 1N4R tau fibrils. Cells were then fixed after 48 hours.
496
497 **Monomeric and fibrillar tau**
498 Full-length human 1N4R tau was expressed and purified as previously described[67]. The purified
499 monomeric tau was dialyzed against PBS buffer containing 1 mM DTT, flash frozen in liquid
500 nitrogen and stored at -80 °C. The concentration of monomeric tau was determined
501 spectrophotometrically using an extinction coefficient at 280 nm of 7575 M^{-1} cm^{-1}. Monomeric
502 1N4R tau was assembled into fibrils at 40 μM in the presence of 10 μM heparin, in PBS buffer
503 containing 1 mM DTT under continuous shaking (600 rpm) for 5 days at 37 °C in an Eppendorf
504 Thermomixer. The quality of 1N4R tau fibrils produced after 5 days was assessed by ThioflavinT
505 binding, sedimentation, and transmission electron microscopy (TEM). The resulting 1N4R tau
506 fibrils were spun at 25 °C and 75 000 g for 30 min. The pelleted fibrils were resuspended in PBS
507 buffer with 1 mM DTT at 50 μM equivalent monomeric tau concentration. 1N4R tau fibrils were
508 labeled by incubation with the 2 molar equivalents of lysine-reactive ATTO 550 (ATTO-TEC,
509 GMBH) for 1 h at room temperature. The unreacted fluorophore was removed by two cycles of
510 centrifugation at 75 000 g for 10 min and resuspension of the pellet in PBS. 1N4R tau fibrils were
511 fragmented by sonication for 5 min in 2-ml Eppendorf tubes in a Vial Tweeter powered by an

512 ultrasonic processor UIS250v (250 W, 2.4 kHz; Hielscher Ultrasonic, Teltow, Germany) to
513 generate fibrillar particles with an average size 50 nm as assessed by TEM analysis. For seeding
514 experiments, either monomeric or fibrillar tau was added directly into the cell culture media to a
515 final concentration of 400 nM. Cells were then fixed after 48 hours.
516
517 **Statistical analysis**
518 Statistical analysis was performed with GraphPad Prism (GraphPad Software, Version 6h and
519 10.1.1). Data was tested for normal distribution by D'Agostino and Pearson omnibus normality
520 test. Data presentation, sample size (number of biological repeats and sample size per repeat and
521 condition), and the applied statistical tests are indicated in the figure legends for each experiment.
522 For all cell culture data, data represents 3 independent replicates with 10 images each replicate.
523 Significance levels: non-significant (n.s.) $p > 0.05$, $*p \leq 0.05$, $**p \leq 0.01$, and $***p \leq 0.001$.
524
525

Acknowledgements

We gratefully acknowledge the technical support of Sarah Wübbel. We extend our gratitude to Dr. Sunil Yeruva for his assistance with the use of the DMI6000 confocal microscope. We appreciate the help of Dr. Hana Nuskova and Dr. Aurelio Teleman (DKFZ, Heidelberg) with the fatty acid conjugation protocol. The tauP301S-Venus expressing HEK293T cell line was kindly provided by Dr. William A. McEwan (Cambridge University)[38]. The pLenti PGK Puro DEST (w529-2) vector was a gift from Dr. Eric Campeau and Dr. Paul Kaufman[62]. We also thank Dr. Bin Liu and Dr. Marja Jäättelä (University of Copenhagen) for sharing the strain BIJ34 and a pPD49.26 expression plasmid coding for sfGFP::LGALS3 and Dr. Xiaochen Wang (Chinese Academy of Sciences, Beijing) for nematodes expressing the qxIs352 transgene. Some strains were provided by the Caenorhabditis Genetics Center (CGC), which is funded by the NIH Office of Research Infrastructure Programs (P40 OD010440).

Author contributions

Conceptualization J.T., C.A.S., C.N.K.

Formal Analysis J.T., C.A.S., N.M.

Funding acquisition R.M., C.N.K.

Investigation J.T., C.A.S., N.M., D.E.

Methodology J.T., C.A.S., N.M.

Project administration C.N.K.

Resources S.B.N.N.

Supervision R.M., C.N.K.

Visualization J.T., C.N.K.

Writing – original draft J.T., C.A.S., C.N.K.

Writing – review & editing J.T., C.A.S., N.M., D.E., R.M., C.N.K.

Declaration of interests

The authors declare no competing interest.

Supplemental information

Document S1. Figures S1–S5.

557 **Data availability**

558 All data supporting the findings of this study are available within the paper and its supplementary
559 information. *C. elegans* strains and plasmids generated in this study are available upon request.

560

561 **References**

562 1. Clavaguera, F., Bolmont, T., Crowther, R.A., Abramowski, D., Frank, S., Probst, A.,
563 Fraser, G., Stalder, A.K., Beibel, M., Staufenbiel, M., et al. (2009). Transmission and
564 spreading of tauopathy in transgenic mouse brain. Nat Cell Biol *11*, 909-913.
565 10.1038/ncb1901.
566 2. Walker, L.C., and Jucker, M. (2024). The prion principle and Alzheimer's disease. Science
567 *385*, 1278-1279. 10.1126/science.adq5252.
568 3. Biel, D., Brendel, M., Rubinski, A., Buerger, K., Janowitz, D., Dichgans, M., Franzmeier,
569 N., and Alzheimer's Disease Neuroimaging, I. (2021). tau-PET and in vivo Braak-staging
570 as prognostic markers of future cognitive decline in cognitively normal to demented
571 individuals. Alzheimer's research & therapy *13*, 137. 10.1186/s13195-021-00880-x.
572 4. Frost, B., Jacks, R.L., and Diamond, M.I. (2009). Propagation of tau misfolding from the
573 outside to the inside of a cell. J Biol Chem *284*, 12845-12852. M808759200
574 10.1074/jbc.M808759200.
575 5. Sanders, D.W., Kaufman, S.K., DeVos, S.L., Sharma, A.M., Mirbaha, H., Li, A., Barker,
576 S.J., Foley, A.C., Thorpe, J.R., Serpell, L.C., et al. (2014). Distinct tau prion strains
577 propagate in cells and mice and define different tauopathies. Neuron *82*, 1271-1288.
578 10.1016/j.neuron.2014.04.047.
579 6. Shrivastava, A.N., Redeker, V., Pieri, L., Bousset, L., Renner, M., Madiona, K., Mailhes-
580 Hamon, C., Coens, A., Buee, L., Hantraye, P., et al. (2019). Clustering of tau fibrils impairs
581 the synaptic composition of alpha3-Na(+)/K(+)-ATPase and AMPA receptors. EMBO J
582 *38*. 10.15252/embj.201899871.
583 7. Caballero, B., Wang, Y., Diaz, A., Tasset, I., Juste, Y.R., Stiller, B., Mandelkow, E.M.,
584 Mandelkow, E., and Cuervo, A.M. (2018). Interplay of pathogenic forms of human tau
585 with different autophagic pathways. Aging cell *17*. 10.1111/acel.12692.
586 8. Menzies, F.M., Fleming, A., and Rubinsztein, D.C. (2015). Compromised autophagy and
587 neurodegenerative diseases. Nat Rev Neurosci *16*, 345-357. 10.1038/nrn3961.
588 9. Nixon, R.A., Wegiel, J., Kumar, A., Yu, W.H., Peterhoff, C., Cataldo, A., and Cuervo,
589 A.M. (2005). Extensive involvement of autophagy in Alzheimer disease: an immuno-
590 electron microscopy study. J Neuropathol Exp Neurol *64*, 113-122.
591 10. Hou, W.C., Massey, L.A., Rhoades, D., Wu, Y., Ren, W., Frank, C., Overkleeft, H.S., and
592 Kelly, J.W. (2024). A PIKfyve modulator combined with an integrated stress response
593 inhibitor to treat lysosomal storage diseases. Proc Natl Acad Sci U S A *121*, e2320257121.
594 10.1073/pnas.2320257121.
595 11. Lim, S.H.Y., Hansen, M., and Kumsta, C. (2024). Molecular Mechanisms of Autophagy
596 Decline during Aging. Cells *13*. 10.3390/cells13161364.
597 12. Caballero, B., Bourdenx, M., Luengo, E., Diaz, A., Sohn, P.D., Chen, X., Wang, C., Juste,
598 Y.R., Wegmann, S., Patel, B., et al. (2021). Acetylated tau inhibits chaperone-mediated
599 autophagy and promotes tau pathology propagation in mice. Nature communications *12*,
600 2238. 10.1038/s41467-021-22501-9.
601 13. Chen, J.J., Nathaniel, D.L., Raghavan, P., Nelson, M., Tian, R., Tse, E., Hong, J.Y., See,
602 S.K., Mok, S.A., Hein, M.Y., et al. (2019). Compromised function of the ESCRT pathway
603 promotes endolysosomal escape of tau seeds and propagation of tau aggregation. J Biol
604 Chem. 10.1074/jbc.RA119.009432.
605 14. Flavin, W.P., Bousset, L., Green, Z.C., Chu, Y., Skarpathiotis, S., Chaney, M.J., Kordower,
606 J.H., Melki, R., and Campbell, E.M. (2017). Endocytic vesicle rupture is a conserved

607 mechanism of cellular invasion by amyloid proteins. Acta Neuropathol. 10.1007/s00401-
608 017-1722-x.
609 15. Tuck, B.J., Miller, L.V.C., Katsinelos, T., Smith, A.E., Wilson, E.L., Keeling, S., Cheng,
610 S., Vaysburd, M.J., Knox, C., Tredgett, L., et al. (2022). Cholesterol determines the
611 cytosolic entry and seeded aggregation of tau. Cell reports *39*, 110776.
612 10.1016/j.celrep.2022.110776.
613 16. Dimou, E., Katsinelos, T., Meisl, G., Tuck, B.J., Keeling, S., Smith, A.E., Hidari, E., Lam,
614 J.Y.L., Burke, M., Lovestam, S., et al. (2023). Super-resolution imaging unveils the self-
615 replication of tau aggregates upon seeding. Cell reports *42*, 112725.
616 10.1016/j.celrep.2023.112725.
617 17. Polanco, J.C., Hand, G.R., Briner, A., Li, C., and Götz, J. (2021). Exosomes induce
618 endolysosomal permeabilization as a gateway by which exosomal tau seeds escape into the
619 cytosol. Acta Neuropathol *141*, 235-256. 10.1007/s00401-020-02254-3.
620 18. Rose, K., Jepson, T., Shukla, S., Maya-Romero, A., Kampmann, M., Xu, K., and Hurley,
621 J.H. (2024). tau fibrils induce nanoscale membrane damage and nucleate cytosolic tau at
622 lysosomes. Proc Natl Acad Sci U S A *121*, e2315690121. 10.1073/pnas.2315690121.
623 19. Kroemer, G., and Jaattela, M. (2005). Lysosomes and autophagy in cell death control.
624 Nature reviews. Cancer *5*, 886-897. 10.1038/nrc1738.
625 20. Sandhof, C.A., Martin, N., Tittelmeier, J., Schlueter, A., Pezzali, M., Schoendorf, D.C.,
626 Lange, T., Reinhardt, P., Ried, J.S., Liang, S., et al. (2024). A Novel *C. elegans* Model for
627 tau Spreading Reveals Genes Critical for Endolysosomal Integrity and Seeded tau
628 Aggregation. bioRxiv, 2024.2011.2013.619586. 10.1101/2024.11.13.619586.
629 21. Breslow, D.K., and Weissman, J.S. (2010). Membranes in balance: mechanisms of
630 sphingolipid homeostasis. Mol Cell *40*, 267-279. 10.1016/j.molcel.2010.10.005.
631 22. Jimenez-Rojo, N., Leonetti, M.D., Zoni, V., Colom, A., Feng, S., Iyengar, N.R., Matile, S.,
632 Roux, A., Vanni, S., Weissman, J.S., and Riezman, H. (2020). Conserved Functions of
633 Ether Lipids and Sphingolipids in the Early Secretory Pathway. Curr Biol *30*, 3775-3787
634 e3777. 10.1016/j.cub.2020.07.059.
635 23. Gault, C.R., Obeid, L.M., and Hannun, Y.A. (2010). An overview of sphingolipid
636 metabolism: from synthesis to breakdown. Adv Exp Med Biol *688*, 1-23. 10.1007/978-1-
637 4419-6741-1_1.
638 24. Futerman, A.H., and Hannun, Y.A. (2004). The complex life of simple sphingolipids.
639 EMBO Rep *5*, 777-782. 10.1038/sj.embor.7400208.
640 25. Czubowicz, K., Jesko, H., Wencel, P., Lukiw, W.J., and Strosznajder, R.P. (2019). The
641 Role of Ceramide and Sphingosine-1-Phosphate in Alzheimer's Disease and Other
642 Neurodegenerative Disorders. Mol Neurobiol *56*, 5436-5455. 10.1007/s12035-018-1448-
643 3.
644 26. van Echten-Deckert, G., and Walter, J. (2012). Sphingolipids: critical players in
645 Alzheimer's disease. Prog Lipid Res *51*, 378-393. 10.1016/j.plipres.2012.07.001.
646 27. Huotari, J., and Helenius, A. (2011). Endosome maturation. EMBO J *30*, 3481-3500.
647 10.1038/emboj.2011.286.
648 28. Yong, J., Villalta, J.E., Vu, N., Kukurugya, M.A., Olsson, N., Lopez, M.P., Lazzari-Dean,
649 J.R., Hake, K., McAllister, F.E., Bennett, B.D., and Jan, C.H. (2024). Impairment of lipid
650 homeostasis causes lysosomal accumulation of endogenous protein aggregates through
651 ESCRT disruption. eLife *12*. 10.7554/eLife.86194.

652 29. Aits, S., Kricker, J., Liu, B., Ellegaard, A.M., Hamalisto, S., Tvingsholm, S., Corcelle-
653 Termeau, E., Hogh, S., Farkas, T., Holm Jonassen, A., et al. (2015). Sensitive detection of
654 lysosomal membrane permeabilization by lysosomal galectin puncta assay. Autophagy *11*,
655 1408-1424. 10.1080/15548627.2015.1063871.
656 30. Hanel, V., Pendleton, C., and Witting, M. (2019). The sphingolipidome of the model
657 organism Caenorhabditis elegans. Chem Phys Lipids *222*, 15-22.
658 10.1016/j.chemphyslip.2019.04.009.
659 31. Cheng, X., Jiang, X., Tam, K.Y., Li, G., Zheng, J., and Zhang, H. (2019). Sphingolipidomic
660 Analysis of C. elegans reveals Development- and Environment-dependent Metabolic
661 Features. Int J Biol Sci *15*, 2897-2910. 10.7150/ijbs.30499.
662 32. D'Auria, L., and Bongarzone, E.R. (2016). Fluid levity of the cell: Role of membrane lipid
663 architecture in genetic sphingolipidoses. J Neurosci Res *94*, 1019-1024.
664 10.1002/jnr.23750.
665 33. Liu, B., Du, H., Rutkowski, R., Gartner, A., and Wang, X. (2012). LAAT-1 is the
666 lysosomal lysine/arginine transporter that maintains amino acid homeostasis. Science *337*,
667 351-354. 10.1126/science.1220281.
668 34. Morck, C., Olsen, L., Kurth, C., Persson, A., Storm, N.J., Svensson, E., Jansson, J.O.,
669 Hellqvist, M., Enejder, A., Faergeman, N.J., and Pilon, M. (2009). Statins inhibit protein
670 lipidation and induce the unfolded protein response in the non-sterol producing nematode
671 Caenorhabditis elegans. Proc Natl Acad Sci U S A *106*, 18285-18290.
672 10.1073/pnas.0907117106.
673 35. Owen, D.M., Rentero, C., Magenau, A., Abu-Siniyeh, A., and Gaus, K. (2011).
674 Quantitative imaging of membrane lipid order in cells and organisms. Nat Protoc *7*, 24-35.
675 10.1038/nprot.2011.419.
676 36. Barucha-Kraszewska, J., Kraszewski, S., and Ramseyer, C. (2013). Will C-Laurdan
677 dethrone Laurdan in fluorescent solvent relaxation techniques for lipid membrane studies?
678 Langmuir *29*, 1174-1182. 10.1021/la304235r.
679 37. Wittrup, A., Ai, A., Liu, X., Hamar, P., Trifonova, R., Charisse, K., Manoharan, M.,
680 Kirchhausen, T., and Lieberman, J. (2015). Visualizing lipid-formulated siRNA release
681 from endosomes and target gene knockdown. Nat Biotechnol *33*, 870-876.
682 10.1038/nbt.3298.
683 38. McEwan, W.A., Falcon, B., Vaysburd, M., Clift, D., Oblak, A.L., Ghetti, B., Goedert, M.,
684 and James, L.C. (2017). Cytosolic Fc receptor TRIM21 inhibits seeded tau aggregation.
685 Proc Natl Acad Sci U S A *114*, 574-579. 10.1073/pnas.1607215114.
686 39. Nachman, E., Wentink, A.S., Madiona, K., Bousset, L., Katsinelos, T., Allinson, K.,
687 Kampinga, H., McEwan, W.A., Jahn, T.R., Melki, R., et al. (2020). Disassembly of tau
688 fibrils by the human Hsp70 disaggregation machinery generates small seeding-competent
689 species. J Biol Chem *295*, 9676-9690. 10.1074/jbc.RA120.013478.
690 40. Yoon, J.H., Seo, Y., Jo, Y.S., Lee, S., Cho, E., Cazenave-Gassiot, A., Shin, Y.S., Moon,
691 M.H., An, H.J., Wenk, M.R., and Suh, P.G. (2022). Brain lipidomics: From functional
692 landscape to clinical significance. Sci Adv *8*, eadc9317. 10.1126/sciadv.adc9317.
693 41. Hornemann, T. (2021). Mini review: Lipids in Peripheral Nerve Disorders. Neurosci Lett
694 *740*, 135455. 10.1016/j.neulet.2020.135455.
695 42. Uranbileg, B., Isago, H., Sakai, E., Kubota, M., Saito, Y., and Kurano, M. (2024).
696 Alzheimer's disease manifests abnormal sphingolipid metabolism. Front Aging Neurosci
697 *16*, 1368839. 10.3389/fnagi.2024.1368839.

43. Corder, E.H., Saunders, A.M., Strittmatter, W.J., Schmechel, D.E., Gaskell, P.C., Small, G.W., Roses, A.D., Haines, J.L., and Pericak-Vance, M.A. (1993). Gene dose of apolipoprotein E type 4 allele and the risk of Alzheimer's disease in late onset families. Science *261*, 921-923. 10.1126/science.8346443.
44. Kosicek, M., Zetterberg, H., Andreasen, N., Peter-Katalinic, J., and Hecimovic, S. (2012). Elevated cerebrospinal fluid sphingomyelin levels in prodromal Alzheimer's disease. Neurosci Lett *516*, 302-305. 10.1016/j.neulet.2012.04.019.
45. Ruiz, M., Devkota, R., Kaper, D., Ruhanen, H., Busayavalasa, K., Radovic, U., Henricsson, M., Kakela, R., Boren, J., and Pilon, M. (2023). AdipoR2 recruits protein interactors to promote fatty acid elongation and membrane fluidity. J Biol Chem *299*, 104799. 10.1016/j.jbc.2023.104799.
46. Zhang, Y., Wang, H., Zhang, J., Hu, Y., Zhang, L., Wu, X., Su, X., Li, T., Zou, X., and Liang, B. (2016). The cytochrome b5 reductase HPO-19 is required for biosynthesis of polyunsaturated fatty acids in Caenorhabditis elegans. Biochim Biophys Acta *1861*, 310-319. 10.1016/j.bbalip.2016.01.009.
47. Fabri, J., de Sa, N.P., Malavazi, I., and Del Poeta, M. (2020). The dynamics and role of sphingolipids in eukaryotic organisms upon thermal adaptation. Prog Lipid Res *80*, 101063. 10.1016/j.plipres.2020.101063.
48. Romanauska, A., and Kohler, A. (2023). Lipid saturation controls nuclear envelope function. Nat Cell Biol *25*, 1290-1302. 10.1038/s41556-023-01207-8.
49. Harayama, T., and Riezman, H. (2018). Understanding the diversity of membrane lipid composition. Nat Rev Mol Cell Biol *19*, 281-296. 10.1038/nrm.2017.138.
50. Rakhra, V., Galappaththy, S.L., Bulchandani, S., and Cabandugama, P.K. (2020). Obesity and the Western Diet: How We Got Here. Mo Med *117*, 536-538.
51. Snowden, S.G., Ebshiana, A.A., Hye, A., An, Y., Pletnikova, O., O'Brien, R., Troncoso, J., Legido-Quigley, C., and Thambisetty, M. (2017). Association between fatty acid metabolism in the brain and Alzheimer disease neuropathology and cognitive performance: A nontargeted metabolomic study. PLoS Med *14*, e1002266. 10.1371/journal.pmed.1002266.
52. Bischoff-Ferrari, H.A., Gangler, S., Wieczorek, M., Belsky, D.W., Ryan, J., Kressig, R.W., Stahelin, H.B., Theiler, R., Dawson-Hughes, B., Rizzoli, R., et al. (2025). Individual and additive effects of vitamin D, omega-3 and exercise on DNA methylation clocks of biological aging in older adults from the DO-HEALTH trial. Nat Aging. 10.1038/s43587-024-00793-y.
53. Shinto, L., Quinn, J., Montine, T., Dodge, H.H., Woodward, W., Baldauf-Wagner, S., Waichunas, D., Bumgarner, L., Bourdette, D., Silbert, L., and Kaye, J. (2014). A randomized placebo-controlled pilot trial of omega-3 fatty acids and alpha lipoic acid in Alzheimer's disease. J Alzheimers Dis *38*, 111-120. 10.3233/JAD-130722.
54. Wood, A.H.R., Chappell, H.F., and Zulyniak, M.A. (2022). Dietary and supplemental long-chain omega-3 fatty acids as moderators of cognitive impairment and Alzheimer's disease. Eur J Nutr *61*, 589-604. 10.1007/s00394-021-02655-4.
55. Brenner, S. (1974). The genetics of Caenorhabditis elegans. Genetics *77*, 71-94.
56. Svensk, E., Stahlman, M., Andersson, C.H., Johansson, M., Boren, J., and Pilon, M. (2013). PAQR-2 regulates fatty acid desaturation during cold adaptation in C. elegans. PLoS Genet *9*, e1003801. 10.1371/journal.pgen.1003801.

743 57. Devkota, R., Svensk, E., Ruiz, M., Stahlman, M., Boren, J., and Pilon, M. (2017). The
744 adiponectin receptor AdipoR2 and its Caenorhabditis elegans homolog PAQR-2 prevent
745 membrane rigidification by exogenous saturated fatty acids. PLoS Genet *13*, e1007004.
746 10.1371/journal.pgen.1007004.
747 58. Sandhof, C.A., Hoppe, S.O., Druffel-Augustin, S., Gallrein, C., Kirstein, J., Voisine, C.,
748 and Nussbaum-Krammer, C. (2020). Reducing INS-IGF1 signaling protects against non-
749 cell autonomous vesicle rupture caused by SNCA spreading. Autophagy *16*, 878-899.
750 10.1080/15548627.2019.1643657.
751 59. Devkota, R., and Pilon, M. (2018). FRAP: A Powerful Method to Evaluate Membrane
752 Fluidity in Caenorhabditis elegans. Bio Protoc *8*, e2913. 10.21769/BioProtoc.2913.
753 60. Svensk, E., Devkota, R., Stahlman, M., Ranji, P., Rauthan, M., Magnusson, F.,
754 Hammarsten, S., Johansson, M., Boren, J., and Pilon, M. (2016). Caenorhabditis elegans
755 PAQR-2 and IGLR-2 Protect against Glucose Toxicity by Modulating Membrane Lipid
756 Composition. PLoS Genet *12*, e1005982. 10.1371/journal.pgen.1005982.
757 61. Chalfie, M., Sulston, J.E., White, J.G., Southgate, E., Thomson, J.N., and Brenner, S.
758 (1985). The neural circuit for touch sensitivity in Caenorhabditis elegans. J Neurosci *5*,
759 956-964.
760 62. Campeau, E., Ruhl, V.E., Rodier, F., Smith, C.L., Rahmberg, B.L., Fuss, J.O., Campisi, J.,
761 Yaswen, P., Cooper, P.K., and Kaufman, P.D. (2009). A versatile viral system for
762 expression and depletion of proteins in mammalian cells. PLoS One *4*, e6529.
763 10.1371/journal.pone.0006529.
764 63. Jeong, J.H., Han, J.S., Jung, Y., Lee, S.M., Park, S.H., Park, M., Shin, M.G., Kim, N.,
765 Kang, M.S., Kim, S., et al. (2023). A new AMPK isoform mediates glucose-restriction
766 induced longevity non-cell autonomously by promoting membrane fluidity. Nature
767 communications *14*, 288. 10.1038/s41467-023-35952-z.
768 64. Oliveira, A.F., Cunha, D.A., Ladriere, L., Igoillo-Esteve, M., Bugliani, M., Marchetti, P.,
769 and Cnop, M. (2015). In vitro use of free fatty acids bound to albumin: A comparison of
770 protocols. Biotechniques *58*, 228-233. 10.2144/000114285.
771 65. Cousin, S.P., Hugl, S.R., Wrede, C.E., Kajio, H., Myers, M.G., Jr., and Rhodes, C.J. (2001).
772 Free fatty acid-induced inhibition of glucose and insulin-like growth factor I-induced
773 deoxyribonucleic acid synthesis in the pancreatic beta-cell line INS-1. Endocrinology *142*,
774 229-240. 10.1210/endo.142.1.7863.
775 66. Nuskova, H., Cortizo, F.G., Schwenker, L.S., Sachsenheimer, T., Diakonov, E.E., Tiebe,
776 M., Schneider, M., Lohbeck, J., Reid, C., Kopp-Schneider, A., et al. (2023). Competition
777 for cysteine acylation by C16:0 and C18:0 derived lipids is a global phenomenon in the
778 proteome. J Biol Chem *299*, 105088. 10.1016/j.jbc.2023.105088.
779 67. Tardivel, M., Begard, S., Bousset, L., Dujardin, S., Coens, A., Melki, R., Buee, L., and
780 Colin, M. (2016). Tunneling nanotube (TNT)-mediated neuron-to neuron transfer of
781 pathological tau protein assemblies. Acta neuropathologica communications *4*, 117.
782 10.1186/s40478-016-0386-4.
783 68. Chitwood, D.J., Lusby, W.R., Thompson, M.J., Kochansky, J.P., and Howarth, O.W.
784 (1995). The glycosylceramides of the nematode Caenorhabditis elegans contain an
785 unusual, branched-chain sphingoid base. Lipids *30*, 567-573. 10.1007/BF02537032.
786 69. Zhang, H., Abraham, N., Khan, L.A., Hall, D.H., Fleming, J.T., and Gobel, V. (2011).
787 Apicobasal domain identities of expanding tubular membranes depend on
788 glycosphingolipid biosynthesis. Nat Cell Biol *13*, 1189-1201. 10.1038/ncb2328.

70. Zhu, H., Shen, H., Sewell, A.K., Kniazeva, M., and Han, M. (2013). A novel sphingolipid-TORC1 pathway critically promotes postembryonic development in Caenorhabditis elegans. eLife *2*, e00429. 10.7554/eLife.00429.
71. Scholz, J., Helmer, P.O., Nicolai, M.M., Bornhorst, J., and Hayen, H. (2021). Profiling of sphingolipids in Caenorhabditis elegans by two-dimensional multiple heart-cut liquid chromatography - mass spectrometry. J Chromatogr A *1655*, 462481. 10.1016/j.chroma.2021.462481.

798 **Figure Legends**

799 **Figure 1. Sphingolipid metabolism dysregulation by KD is linked to of endolysosomal vesicle**
800 **rupture.**

801 **(A)** General overview of sphingolipid metabolism with a particular focus on the genes identified
802 in the screen we performed. Sphingolipids constitute a group of amphipathic lipids featuring a
803 polar head group and a sphingoid base backbone that is N-acetylated with a (very) long-chain fatty
804 acid ((V)LCFA) side chain. In contrast to mammals, where the sphingoid base is conventionally
805 derived from palmitic acid and serine, *C. elegans* sphingolipids usually contain a characteristic
806 C17iso branched chain sphingoid base [68-70]. Its synthesis involves the branched chain FA (BCFA)
807 elongation pathway to yield C15iso-CoA, which then condensates with L-serine to form 3-
808 ketosphinganine. This reaction is catalyzed by serine palmitoyltransferase (encoded by *sptl-1*, *-2*,
809 and *-3*). The serine incorporator (SERINC) protein family (encoded by *R11H6.2*) is believed to
810 assist in the incorporation of L-serine into specific membranes. 3-ketodihydrosphingosine
811 reductase (KDSR, in *C. elegans* predicted to be encoded by Y37E11AM.3) then catalyzes the
812 reduction of 3-keto sphinganine to sphinganine. The (V)LCFA side chain is primarily comprised
813 of a straight saturated FA chain, ranching from 20-26 carbon atoms in length, with or without
814 hydroxylation [30,71]. It can be also derived from BCFAs, such as C15iso and C17iso [68,69]. However,
815 most of the side chain FA moieties originate from palmitoyl-CoA via the canonical de novo FA
816 biosynthesis pathway, involving the sequential addition of C2 moieties from malonyl-CoA through
817 the LCFA elongation cycle [68,69]. Each elongation cycle comprises four reactions (condensation,
818 reduction, dehydration, reduction), with the third reaction requiring very-long-chain (3R)-3-
819 hydroxyacyl-CoA dehydratase (encoded by *hpo-8*) [69]. Finally, ceramide synthases (encoded by
820 *hyl-1* and *hyl-2*) catalyze the addition of various acyl side chains to the sphingoid base to yield
821 dihydroceramide, which is then desaturated to ceramide. The latter reaction is catalyzed by
822 dihydroceramide desaturases, which require electrons from NAD(P)H provided by cytochrome b5
823 reductases (encoded by *hpo-19* and *T05H4.4*). All complex sphingolipids, such as sphingomyelin
824 and glycosphingolipids (including cerebrosides and gangliosides) originate from ceramide.
825 Degradation of complex sphingolipids takes place in the lysosome. Essential for this process are
826 saposins or sphingolipid activator proteins (PSAPs, encoded by *spp-10*), which serve as crucial
827 bridges between the lipid substrate and hydrophilic hydrolases. Glucocerebrosidases (encoded by
828 *gba-1*, *gba-2*, *gba-3*, and *gba-4*) hydrolyse glucosylceramide into ceramide and glucose.

829 Sphingosine may be either recycled and metabolized back into ceramide or phosphorylated by
830 sphingosine kinase (encoded by *sphk-1*) to generate sphingosine-1-phosphate (S1P). S1P lyase
831 (encoded by *spl-1*) irreversibly cleaves S1P into phospho-ethanolamine and hexadecenal. The *C.*
832 *elegans* genes identified in the primary screen, along with their human orthologs, are framed with
833 color. Genes identified in subsequent co-RNAi experiments and their human orthologs are framed
834 in gray.
835 **(B)** Schematic of lysosomal rupture detected by the galectin puncta assay.
836 **(C)** Widefield fluorescence images of animals expressing hypodermal sfGFP::LGALS3.
837 Numerous foci are visible upon RNAi-mediated KD of sphingolipid metabolisms genes. Zoomed
838 in image is indicated in overview image by a white box.
839 **(D)** Mean percentage of animals positive for lysosomal rupture (defined as three or more
840 sfGFP::LGALS3 foci in the hypodermis). Data shown as means of three technical replicate plates
841 with 17-30 animals per plate ± SEM. Statistical analysis comparing RNAi conditions to the empty
842 vector control (EV ctrl) was done using one-way ANOVA with Dunnett's post-hoc test. *** = p
843 < 0.001.
844
845 **Figure 2. Knockdown of genes involved in sphingolipid metabolism decreases lysosomal**
846 **membrane fluidity.**
847 **(A)** Representative confocal single plane images from a FRAP experiment in animals expressing
848 a mCherry tagged Lysosomal Lysine/Arginine Transporter 1 (LAAT-1::mCherry) in the
849 hypodermis grown either on empty vector control (EV ctrl), *spl-1* or *sphk-1* RNAi plates. Dashed
850 circles outline the bleach spots.
851 **(B)** Combined FRAP curves of LAAT-1::mCherry in hypodermal lysosomal membranes. Curves
852 are normalized to the pre-bleach intensity as 100% and the first post-bleach intensity as 0%.
853 **(C, D)** Increase (C) in the mean time until half of the maximal signal is recovered (t_{half},) and
854 decrease (D) in the maximal % recoverable fluorescence values upon KD of *sphk-1* and *spl-1*
855 indicate a reduction in lysosomal membrane fluidity.
856 **(E)** FRAP curves of LAAT-1::mCherry in hypodermal lysosomal membranes of animals grown
857 either on empty vector or the indicated RNAi plates. Curves are normalized to the pre-bleach
858 intensity set as 100% and the first post-bleach intensity as 0%.
859 **(F)** Mean t_{half} upon KD of sphingolipid metabolism genes.

860 **(G)** Maximal % recoverable fluorescence values upon KD of sphingolipid metabolism genes.
861 **(H)** Representative confocal single plane images from a FRAP experiment in animals expressing
862 prenylated GFP for lipid membrane anchorage in the intestine.
863 **(I)** Combined FRAP curves of prenylated GFP enriched on the intestinal plasma membrane of
864 animals grown either on empty vector, *sphk-1* or *spl-1* RNAi plates. Curves are normalized to the
865 pre-bleach intensity as 100% and the first post-bleach intensity as 0%.
866 **(J, K)** Mean t_{half} (J) and maximal % recoverable fluorescence values (K). Data represented as
867 means ± SEM of 5 – 12 FRAP measurements per condition collected in five biological replicates.
868 Statistical analysis comparing RNAi conditions to the empty vector control was done using one-
869 way ANOVA with Dunnett's post-hoc test. n.s.: not significant, * = $p < 0.05$, ** = $p < 0.01$, ***
870 = $p < 0.001$
871
872 **Figure 3. KD of SPHK2 and aggregated tau reduces membrane fluidity leading to lysosomal**
873 **rupture.**
874 **(A)** Scheme of the fluorescence properties of C-Laurdan. The dye is excited using illumination at
875 405 nm. The dye fluoresces with a peak emission wavelength around 450 nm (red) when residing
876 in the ordered phase and ~500 nm in the disordered phase (blue). Two-channel acquisition is
877 conducted in the wavelength bands indicated by shaded boxes.
878 **(B)** Pseudo-color images showing the GP index of C-Laurdan dye at each pixel position in
879 HEK293T cells upon KD of SPHK2.
880 **(C)** Increase in GP Index of HEK293T cells upon KD of SPHK2. Statistical analysis was done
881 using one-way ANOVA with Bonferroni's post-hoc test.
882 **(D)** Max. intensity projection of confocal z-stacks of HEK293T cells expressing sfGFP-LGALS3
883 upon KD of SPHK2 and seeding with 1N4R tau fibrils.
884 **(E)** Average number of foci per number of cells. n= 3 independent experiments, 10 images each.
885 Statistical analysis done using oKruskal-Wallis with a Dunn's post-hoc test.
886 **(F)** Quantification of the percentage of animals with ≥ 3 hypodermal sfGFP::LGALS3 foci,
887 representing endolysosomal damage, expressing either the $F3^{\Delta K281}$::mCherry (red) or only the
888 mCherry tag (grey) in touch receptor neurons under knockdown of the indicated genes.
889 **(G)** Dilution of the indicated RNAi cultures with the empty vector control culture was done to
890 reduce the strength of the knockdown. Data represented as mean ± SEM. Besides knockdown of

891 *sphk-1* in **C** n = 3 - 7 with **F** 40 – 50 or **G** 20 – 30 animals per replicate. Since even a dilution down
892 to 5% of the *sphk-1* RNAi resulted in 100% of animals being scored as positive in two independent
893 replicates this condition was not repeated further. Statistical analysis comparing RNAi conditions
894 to the empty vector control done using one-way ANOVA with Dunnett's post-hoc test.
895 **(H)** Worms expressing $F3^{\Delta K281}$::mCherry or mCherry in touch receptor neurons stained with C-
896 Laurdan. The mCherry signal was used to select a region of interest (ROI) around the soma of the
897 posterior touch receptor neurons (PLM) to determine the GP Index.
898 **(I)** Increase in rigidity of membranes in animals expressing $F3^{\Delta K281}$::mCherry compared to
899 mCherry. Statistical analysis was done using a t-test. n=4, total of at least 28 worms.
900 **(J)** Pseudocolored HEK293T cells exposed to tau 1N4R fibrils visualizing the C-Laurdan dye GP
901 Index.
902 **(K)** Increase rigidity of membranes of cells seeded with tau fibrils as indicated by the GP index.
903 **(L)** GP index of cells seeded with monomeric tau. Statistical analysis for C-Laurdan in cells was
904 done using a t-test. n= 3 independent experiments, 10 images each. Scale bar 10 µm. n.s.: not
905 significant, * = $p < 0.05$, ** = $p < 0.01$, *** = $p < 0.001$.
906
907 **Figure 4. Saturated fatty acids decrease membrane fluidity and exacerbate seeded tau**
908 **aggregation.**
909 **(A)** Left: saturated fatty acid membrane scheme. Right: pseudocolored HEK293T cells pre-loaded
910 with 50 µM PA conjugated to BSA (BSA-PA) displaying the C-Laurdan dye GP Index.
911 **(B)** GP Index indicates increased rigidity of membranes with BSA-PA. Statistical analysis was
912 done using the Mann-Whitney-test. n= 3 independent experiments, 10 images each.
913 **(C)** Pseudocolored HEK293T cells pre-loaded with BSA-PA and seeded with 1N4R tau fibrils.
914 **(D)** GP Index indicates an additive impact of tau fibrils on membrane rigidity when added to
915 HEK293T cells pre-loaded with BSA-PA. Statistical analysis was done using t-test. n= 3
916 independent experiments, 10 images each.
917 **(E)** Quantification of hypodermal sfGFP-LGALS3 foci in animals grown on plates supplemented
918 with PA reveal an increase in lysosomal rupture. Statistical analysis was done using Mann-
919 Whitney test. n= 3 independent experiments, 15 worms per replicate.
920 **(F)** Max. intensity projection of confocal z-stacks of HEK293T cells expressing sfGFP-LGALS3
921 pre-loaded with BSA-PA and seeded with 1N4R tau fibrils.

922 **(G)** Quantification of sfGFP-LGALS3 foci in HEK293T cells following indicated treatments.
923 **(H)** Max. intensity projection of confocal z-stacks of Venus-tagged full-length P301S tau
924 biosensor cells pre-loaded with BSA-PA and seeded with 1N4R tau fibrils.
925 **(I)** Quantification of Venus-P301S tau foci following indicated treatments. Statistical analysis
926 comparing BSA + tau to other conditions was done using one-way ANOVA with Dunnett's post-
927 hoc test. n= 3 independent experiments, 10 images each. * = $p < 0.05$, ** = $p < 0.01$, *** = $p <$
928 0.001. Scale bar 10 µm.
929
930 **Figure 5. PUFA supplementation restores lysosomal membrane integrity and reduces seeded**
931 **tau aggregation and toxicity.**
932 **(A)** Left: unsaturated fatty acid membrane scheme. Right: C-Laurdan GP Index of HEK293T cells
933 pre-loaded with 150 µM ALA conjugated to BSA (BSA-ALA) indicating an increase in membrane
934 fluidity. Statistical analysis was done with a t-test. n= 3 independent experiments, 10 images each.
935 **(B)** Pseudocolored HEK293T cells pre-loaded with BSA-ALA and seeded with 1N4R tau fibrils.
936 **(C)** GP Index indicates that BSA-ALA reduces tau-induced rigidification of the membrane.
937 Statistical analysis was done using the Mann-Whitney U-test. n= 3 independent experiments, 10
938 images each.
939 **(D)** Max. intensity projection of confocal z-stacks of HEK293T cells expressing sfGFP-LGALS3
940 pre-loaded with BSA-ALA and seeded with 1N4R tau fibrils. Scale bar 10 µm.
941 **(E)** Quantification of sfGFP-LGALS3 foci following indicated treatments. n= 3 independent
942 experiments, 10 images each.
943 **(F)** Max. intensity projection of confocal z-stacks of tau-Venus biosensor cell line pre-loaded with
944 BSA-ALA and seeded with 1N4R tau fibrils. Scale bar 10 µm.
945 **(G)** Quantification of tau-Venus foci following indicated treatments. Statistical analysis
946 comparing BSA + tau to other conditions was done using Kruskal-Wallis with Dunn's post-hoc
947 test. n = 3 independent experiments, 10 images each.
948 **(H)** Posterior response to touch during aging of animals expressing $F3^{\Delta K281}$::mCherry grown on
949 plates supplemented with ALA or only the ethanol solvent. Statistical analysis was done using
950 two-way ANOVA with Bonferroni's multiple comparison test.
951 **(I)** Max. intensity projection of confocal z-stacks of day 6 old animals expressing
952 $F3^{\Delta K281}$::mCherry.

953 **(J)** Neurotoxicity score of PLM neurons of animals grown on control or ALA plates. Statistical
954 analysis was done using 2-way ANOVA with a Holm-Sidak's multiple comparison test. n= 3
955 independent experiments, 15 worms per replicate. Scale bar 20 µm. * = $p < 0.05$, ** = $p < 0.01$,
956 *** = $p < 0.001$.
957

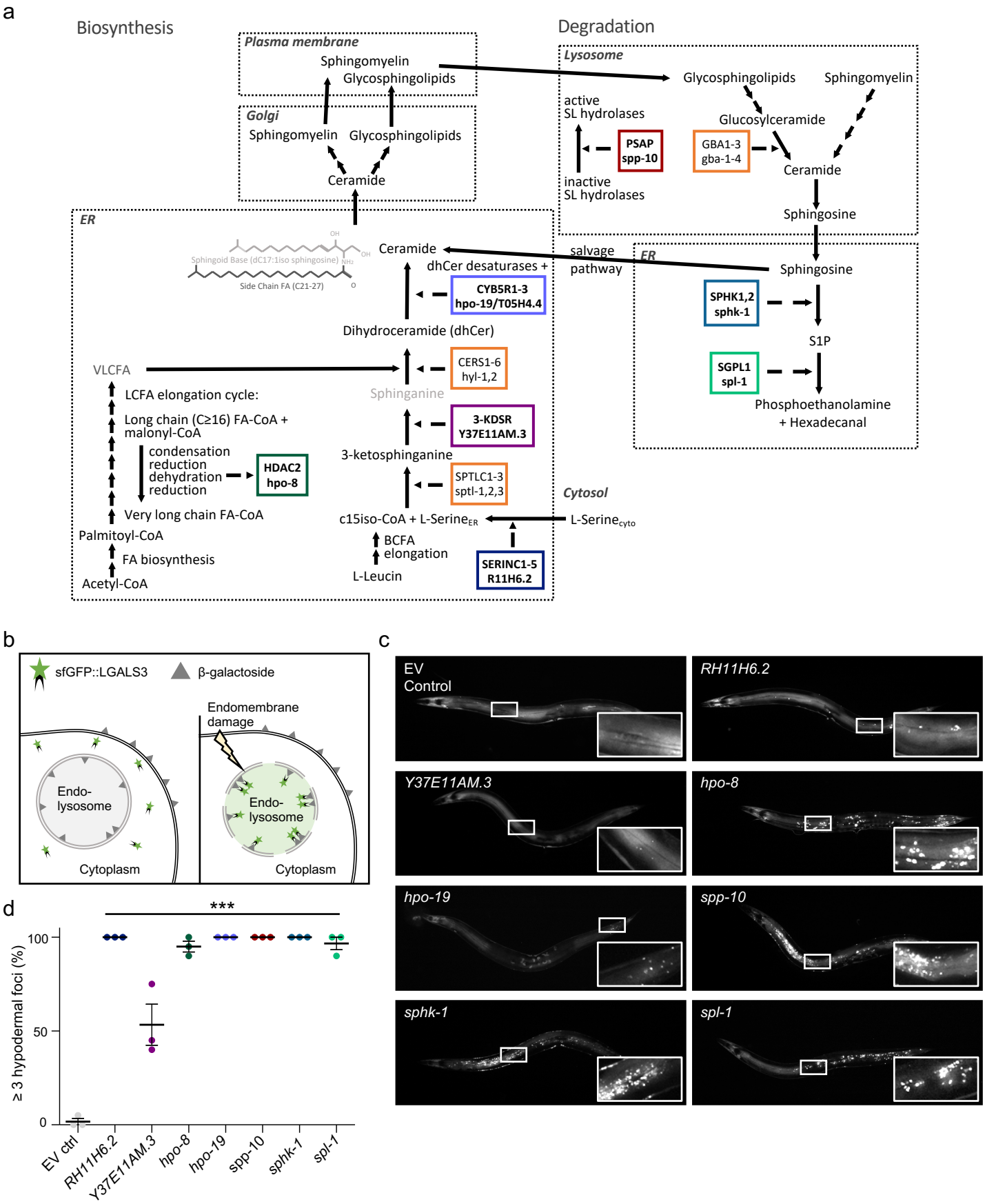
a
Biosynthesis
Degradation
Plasma membrane
Sphingomyelin
Glycosphingolipids
Golgi
Sphingomyelin
Glycosphingolipids
Ceramide
Lysosome
Glycosphingolipids
Sphingomyelin
active
SL hydrolases
PSAP
spp-10
inactive
SL hydrolases
Glucosylceramide
GBA1-3
gba-1-4
Ceramide
Sphingosine
ER
Sphingoid Base (dC17:1iso sphingosine)
Side Chain FA (C21-27)
Ceramide
dhCer desaturases +
CYB5R1-3
hpo-19/T05H4.4
Dihydroceramide (dhCer)
salvage
pathway
ER
Sphingosine
SPHK1,2
sphk-1
S1P
SGPL1
spl-1
Phosphoethanolamine
+ Hexadecanal
VLCFA
CERS1-6
hyl-1,2
Sphinganine
LCFA elongation cycle:
Long chain (C≥16) FA-CoA +
malonyl-CoA
condensation
reduction
dehydration
reduction
HDAC2
hpo-8
3-KDSR
Y37E11AM.3
3-ketosphinganine
SPTLC1-3
sptl-1,2,3
Cytosol
Very long chain FA-CoA
c15iso-CoA + L-Serine$_{ER}$
L-Serine$_{cyto}$
Palmitoyl-CoA
BCFA
elongation
FA biosynthesis
L-Leucin
SERINC1-5
R11H6.2
Acetyl-CoA

b
sfGFP::LGALS3
β-galactoside
Endomembrane
damage
Endo-
lysosome
Endo-
lysosome
Cytoplasm
Cytoplasm

d
***
≥ 3 hypodermal foci (%)
100
50
0
EV ctrl
RH11H6.2
Y37E11AM.3
hpo-8
hpo-19
spp-10
sphk-1
spl-1

c
EV
Control
RH11H6.2
Y37E11AM.3
hpo-8
hpo-19
spp-10
sphk-1
spl-1

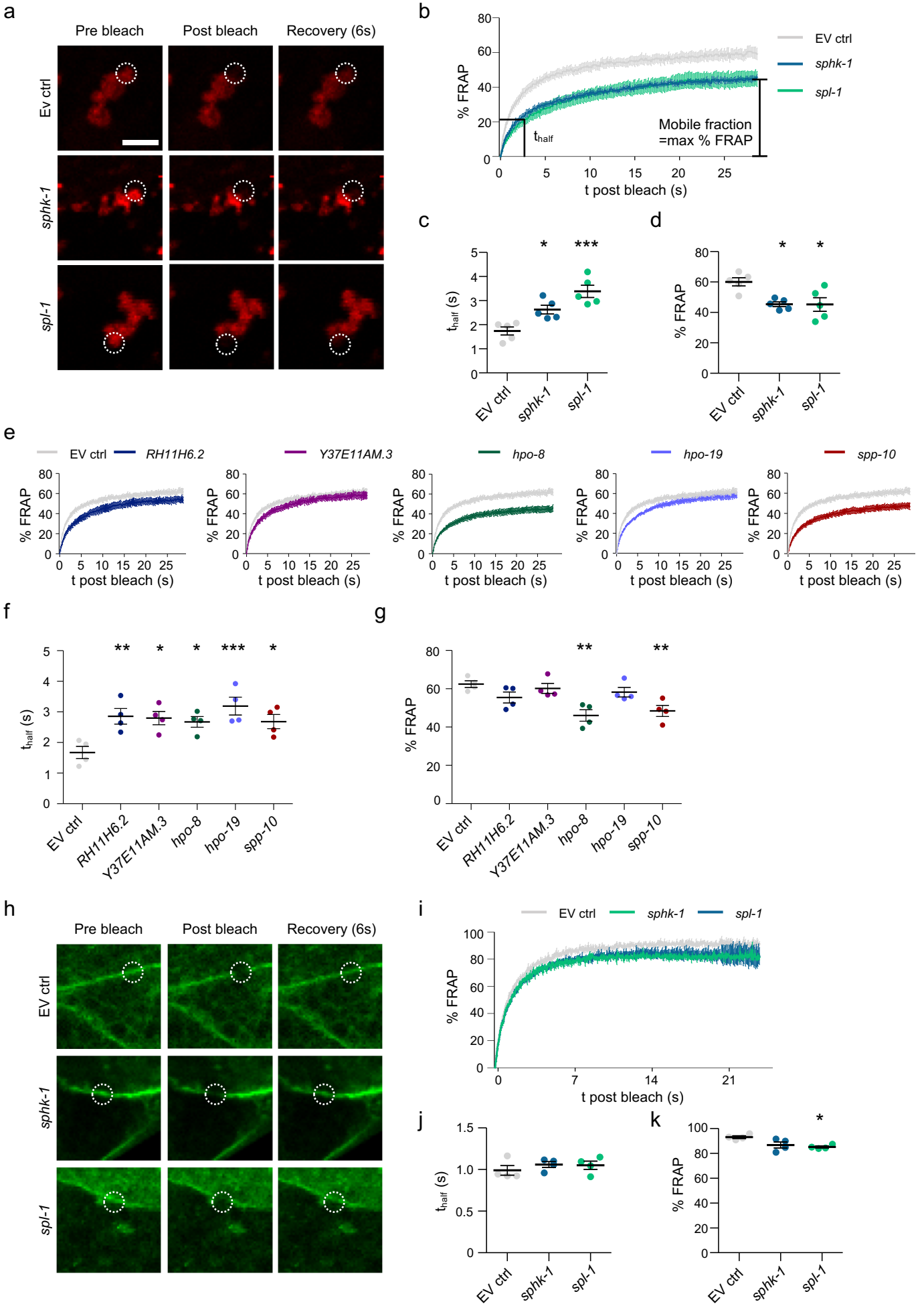
a
Pre bleach
Post bleach
Recovery (6s)
Ev ctrl
sphk-1
spl-1
b
% FRAP
t post bleach (s)
EV ctrl
sphk-1
spl-1
t_{half}
Mobile fraction
=max % FRAP
c
t_{half} (s)
EV ctrl
sphk-1
spl-1
d
% FRAP
e
EV ctrl
RH11H6.2
Y37E11AM.3
hpo-8
hpo-19
spp-10
f
t_{half} (s)
g
% FRAP
h
Pre bleach
Post bleach
Recovery (6s)
EV ctrl
sphk-1
spl-1
i
% FRAP
t post bleach (s)
j
t_{half} (s)
k
% FRAP

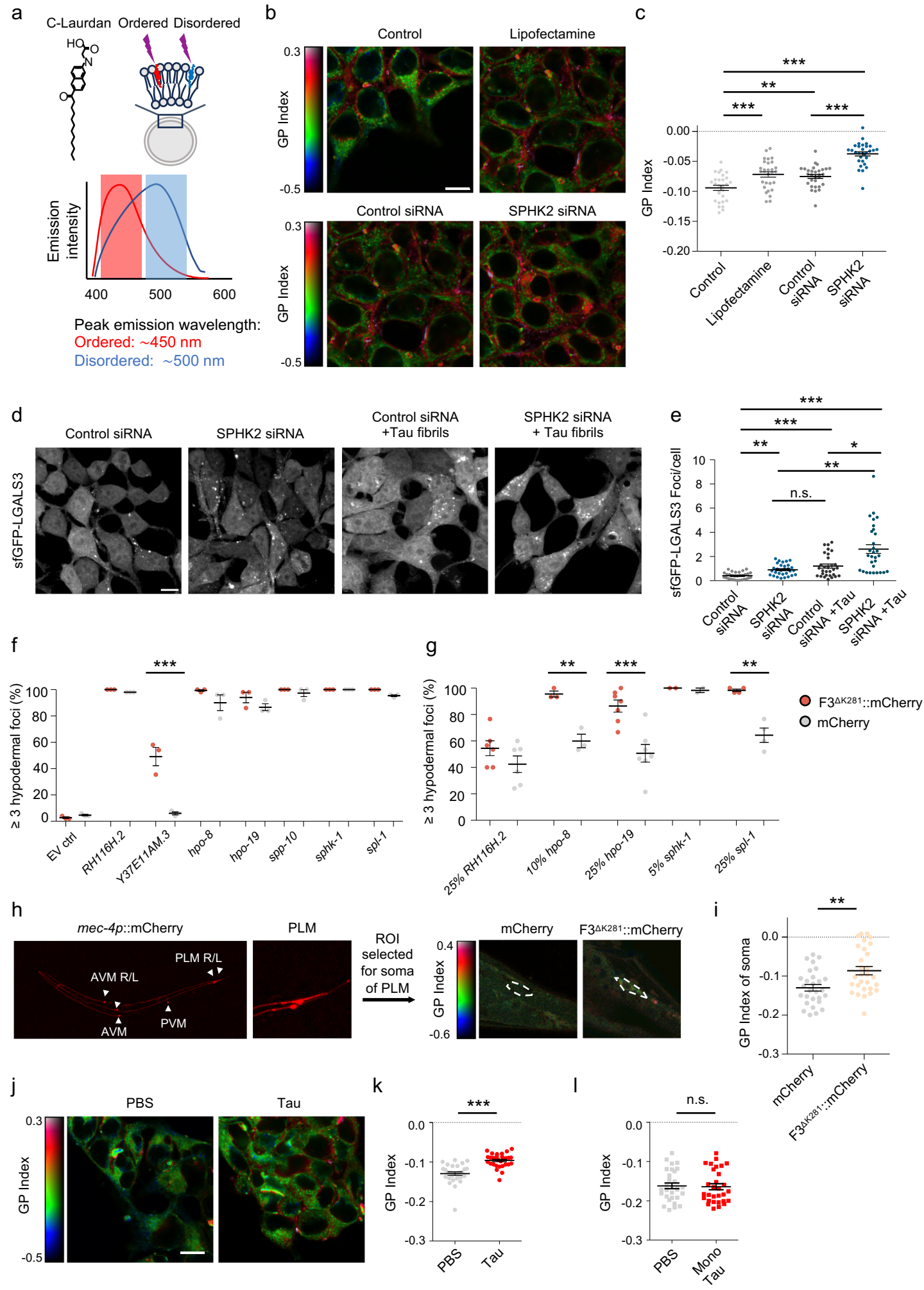
a
C-Laurdan
Ordered
Disordered
Emission intensity
400
500
600
Peak emission wavelength:
Ordered: ~450 nm
Disordered: ~500 nm
b
Control
Lipofectamine
Control siRNA
SPHK2 siRNA
GP Index
0.3
-0.5
c
GP Index
0.00
-0.05
-0.10
-0.15
-0.20
***
**
Control
Lipofectamine
Control siRNA
SPHK2 siRNA
d
Control siRNA
SPHK2 siRNA
Control siRNA +Tau fibrils
SPHK2 siRNA + Tau fibrils
sfGFP-LGALS3
e
sfGFP-LGALS3 Foci/cell
n.s.
*
Control siRNA
SPHK2 siRNA
Control siRNA +Tau
SPHK2 siRNA +Tau
f
≥ 3 hypodermal foci (%)
EV ctrl
RH116H.2
Y37E11AM.3
hpo-8
hpo-19
spp-10
sphk-1
spl-1
g
≥ 3 hypodermal foci (%)
25% RH116H.2
10% hpo-8
25% hpo-19
5% sphk-1
25% spl-1
F3ΔK281::mCherry
mCherry
h
mec-4p::mCherry
PLM
PLM R/L
AVM R/L
AVM
PVM
ROI selected for soma of PLM
mCherry
F3ΔK281::mCherry
GP Index
0.4
-0.6
i
GP Index of soma
mCherry
F3ΔK281::mCherry
j
PBS
Tau
GP Index
k
GP Index
PBS
Tau
l
GP Index
n.s.
PBS
Mono Tau

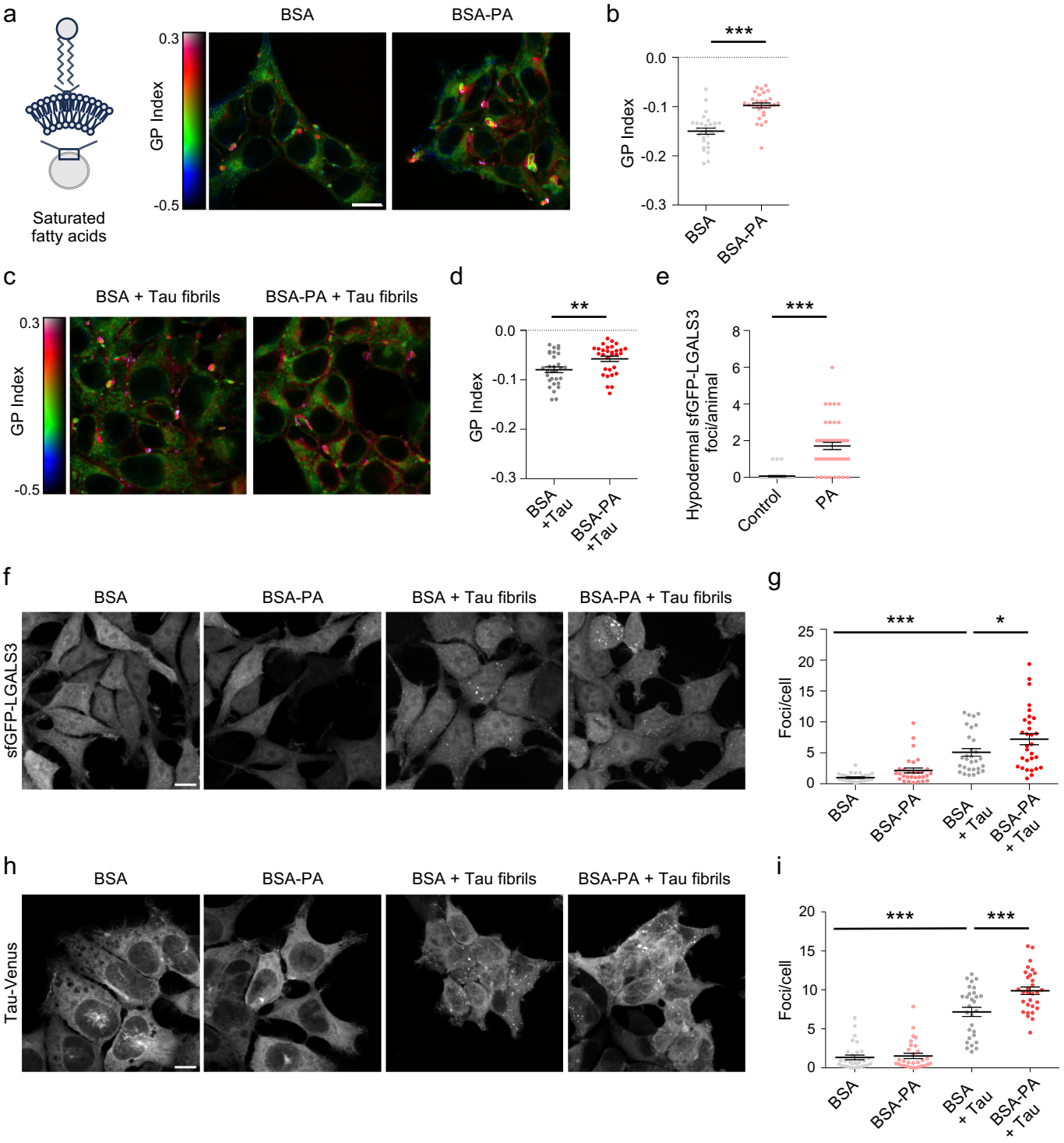
a
Saturated fatty acids
BSA
BSA-PA
GP Index
0.3
-0.5
b
***
GP Index
0.0
-0.1
-0.2
-0.3
BSA
BSA-PA
c
BSA + Tau fibrils
BSA-PA + Tau fibrils
GP Index
0.3
-0.5
d
**
GP Index
0.0
-0.1
-0.2
-0.3
BSA +Tau
BSA-PA +Tau
e
***
Hypodermal sfGFP-LGALS3 foci/animal
8
6
4
2
0
Control
PA
f
BSA
BSA-PA
BSA + Tau fibrils
BSA-PA + Tau fibrils
sfGFP-LGALS3
g
***
*
Foci/cell
25
20
15
10
5
0
BSA
BSA-PA
BSA + Tau
BSA-PA + Tau
h
BSA
BSA-PA
BSA + Tau fibrils
BSA-PA + Tau fibrils
Tau-Venus
i
***
***
Foci/cell
20
15
10
5
0
BSA
BSA-PA
BSA + Tau
BSA-PA + Tau

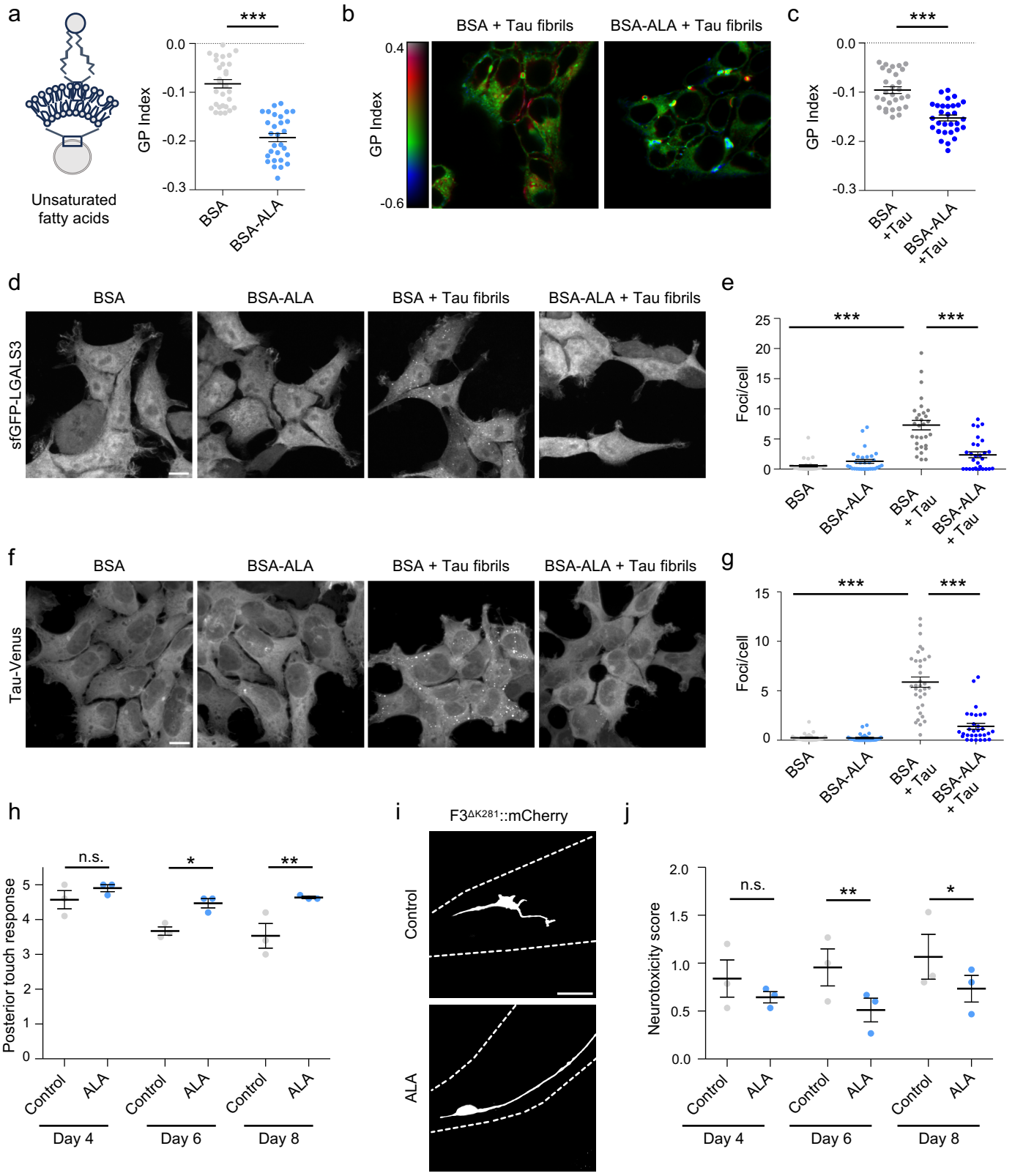
a
Unsaturated fatty acids
GP Index
0.0
-0.1
-0.2
-0.3
***
BSA
BSA-ALA
b
BSA + Tau fibrils
BSA-ALA + Tau fibrils
GP Index
0.4
-0.6
c
GP Index
0.0
-0.1
-0.2
-0.3
***
BSA +Tau
BSA-ALA +Tau
d
BSA
BSA-ALA
BSA + Tau fibrils
BSA-ALA + Tau fibrils
sfGFP-LGALS3
e
Foci/cell
25
20
15
10
5
0
***
***
BSA
BSA-ALA
BSA + Tau
BSA-ALA + Tau
f
BSA
BSA-ALA
BSA + Tau fibrils
BSA-ALA + Tau fibrils
Tau-Venus
g
Foci/cell
15
10
5
0
***
***
BSA
BSA-ALA
BSA + Tau
BSA-ALA + Tau
h
Posterior touch response
5
4
3
2
1
0
n.s.
*
**
Control
ALA
Control
ALA
Control
ALA
Day 4
Day 6
Day 8
i
F3ΔK281::mCherry
Control
ALA
j
Neurotoxicity score
2.0
1.5
1.0
0.5
0.0
n.s.
**
*
Control
ALA
Control
ALA
Control
ALA
Day 4
Day 6
Day 8